

---

# Data-Efficient Time-Dependent PDE Surrogates: Graph Neural Simulators vs. Neural Operators

---

**Dibyajyoti Nayak**

Department of Civil and Systems Engineering  
Johns Hopkins University  
Baltimore, MD, 21218  
dnayak2@jh.edu

**Somdatta Goswami**

Department of Civil and Systems Engineering  
Johns Hopkins University  
Baltimore, MD, 21218  
somdatta@jhu.edu

## Abstract

Developing accurate, data-efficient surrogate models is central to advancing AI for Science. Neural operators (NOs), which approximate mappings between infinite-dimensional function spaces using conventional neural architectures, have gained popularity as surrogates for systems driven by partial differential equations (PDEs). However, their reliance on large datasets and limited ability to generalize in low-data regimes hinder their practical utility. We argue that these limitations arise from their global processing of data, which fails to exploit the local, discretized structure of physical systems. To address this, we propose Graph Neural Simulators (GNS) as a principled surrogate modeling paradigm for time-dependent PDEs. GNS leverages message-passing combined with numerical time-stepping schemes to learn PDE dynamics by modeling the instantaneous time derivatives. This design mimics traditional numerical solvers, enabling stable long-horizon rollouts and strong inductive biases that enhance generalization. We rigorously evaluate GNS on four canonical PDE systems: (1) 2D scalar Burgers', (2) 2D coupled Burgers', (3) 2D Allen–Cahn, and (4) 2D nonlinear shallow-water equations, comparing against state-of-the-art NOs including Deep Operator Network (DeepONet) and Fourier Neural Operator (FNO). Results demonstrate that GNS is markedly more data-efficient, achieving  $< 1\%$  relative  $L_2$  error using only 3% of available trajectories, and exhibits dramatically reduced error accumulation over time (82.5% lower autoregressive error than FNO, 99.9% lower than DeepONet). To choose the training data, we introduce a PCA+KMeans trajectory selection strategy. These findings provide compelling evidence that GNS, with its graph-based locality and solver-inspired design, is the most suitable and scalable surrogate modeling framework for AI-driven scientific discovery. Code and data are available at the project repository: [https://github.com/Centrum-IntelliPhysics/GNS\\_vs\\_NOs.git](https://github.com/Centrum-IntelliPhysics/GNS_vs_NOs.git).

## 1 Introduction

Time-dependent partial differential equations (PDEs) are central to the mathematical modeling of a wide range of physical phenomena, from fluid mechanics and material physics to acoustics and geosciences. Classical numerical solvers such as finite difference, finite volume, and finite element methods remain the workhorse for obtaining accurate solutions. However, their computational cost grows rapidly with problem size and complexity. Large-scale simulations can demand millions of core-hours on supercomputers, making them prohibitive in tasks such as design optimization, uncertainty quantification, inverse modeling, or real-time control, which require repeated evaluations under varying conditions. In such scenarios, relying solely on traditional solvers is infeasible.

To address this issue, surrogate modeling has emerged as a powerful alternative. By approximating the behavior of high-fidelity simulations, surrogates can deliver rapid and reasonably accurate solutions at

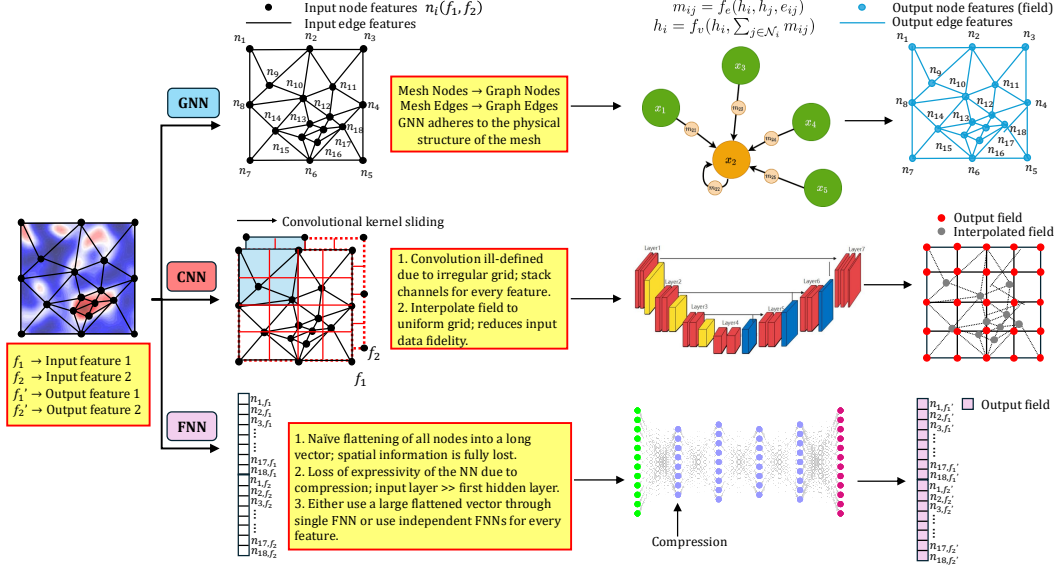


Figure 1: Comparison of neural network architectures for neural operators in scientific applications. Fully connected neural networks (FNNs) flatten mesh data, discarding spatial structure and compressing high-dimensional inputs into narrow hidden layers, which limits expressivity. Convolutional neural networks (CNNs) require interpolation to uniform grids at both input and output, sacrificing fidelity on unstructured (adaptive) meshes and introducing errors tied to interpolation order. Graph neural networks (GNNs), by contrast, natively represent mesh nodes and edges as graphs, preserving geometry, topology, and physical interactions. Their intrinsic alignment with mesh discretizations, ability to exploit locality, and data efficiency make GNNs the natural choice for Scientific Machine Learning, where irregular geometries and fine discretizations are the norm.

a fraction of the computational cost. Early approaches to surrogate modeling were primarily physics-based reduced-order methods, which achieved success in simpler problem settings but struggled with nonlinear, high-dimensional, or complex systems [1, 2, 3, 4, 5, 6]. More recently, machine learning approaches, in particular, neural operators (NOs) [7, 8, 9, 10, 11, 12, 13, 14] have gained traction for learning mappings between infinite-dimensional input–output function spaces. Popular architectures among NOs such as the deep operator network (DeepONet) [7] and Fourier neural operator (FNO) [15] offer mesh-independent PDE solvers that are scalable to high-dimensional systems, representing a paradigm shift away from traditional numerical pipelines. While NOs can provide rapid inference across a parametric sweep of input conditions, they often require large amounts of training data and can therefore exhibit poor generalization in data-scarce or limited data regimes. One approach to mitigate this limitation is to incorporate physics-informed strategies [16, 17, 8, 18, 19] which explicitly enforce that the network’s predictions satisfy the underlying PDE structure, along with initial and boundary conditions. Such physics-informed neural operators have shown promise, but they come with their own set of challenges. In particular, they require explicit knowledge of the governing PDE and accurate specification of initial and boundary conditions – information that may not always be available in realistic or complex systems. Moreover, the optimization of physics-informed loss terms often demands careful hyperparameter tuning, making training a non-trivial task [20, 21]. Furthermore, architectures like FNNs [22] or CNNs [23], which NOs often build upon, exacerbate these issues: fully connected networks treat the domain as flattened vectors, discarding spatial structure, while CNNs assume uniform discretizations and rely on kernels that aggregate information in ways that do not reflect physical locality (see Fig. 1). As a result, such models can fail to capture the inherently local interactions *e.g.*, flux exchanges between neighboring elements that drive PDE-governed dynamics. This mismatch limits their utility in real-world physical applications like fluid flow around complex geometries, deformable materials, phase boundaries, or environmental modeling.

Graph-based learning offers a compelling solution for leveraging local interactions by discretizing computational domains as graphs, where nodes correspond to spatial locations and edges encode local connectivity. This representation naturally handles non-uniform meshes and irregular geometries while aligning with the local interactions inherent in physical systems (see Fig. 1). Such non-uniform structures are ubiquitous in scientific computing, appearing in mesh-based simulations (finite element and adaptive meshes), particle-based methods (molecular dynamics and smoothed particle hydrodynamics), and point cloud data from geophysical or astronomical observations. In these applications, simulation domains are often defined on unstructured or dynamically deforming meshes, making traditional convolutional architectures poorly suited for direct data processing. Graph Neural Networks (GNNs) have emerged as a powerful framework for learning on graph-structured data through iterative message-passing mechanisms that aggregate information from neighboring nodes, effectively capturing both local dependencies and global structural patterns [24, 25, 26, 27]. This inherent flexibility enables GNNs to model physical systems with adaptive meshes or spatially heterogeneous properties by learning dynamics directly from data, without requiring structured grids or explicit knowledge of governing PDEs. Unlike CNNs or FNNs, which rely on regular data structures, GNNs propagate information through explicit connectivity patterns, allowing them to capture fine-grained local gradients while maintaining sensitivity to long-range dependencies. This natural alignment with PDE physics makes GNN-based surrogates remarkably data-efficient, capable of learning solution operators from relatively small datasets while generalizing across varying resolutions and scaling effectively to high-dimensional systems.

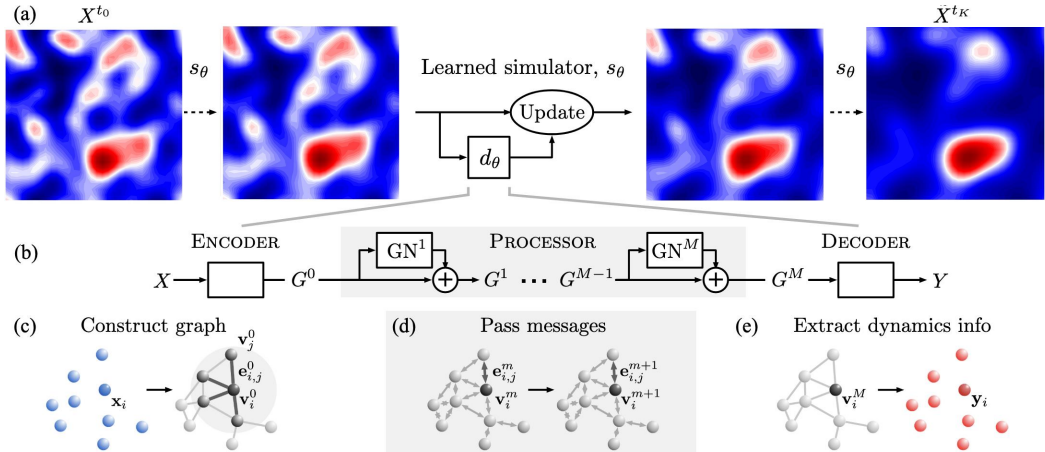


Figure 2: A schematic of the Graph Neural Simulator (GNS) architecture (adapted from [28]).

Building on the flexibility of GNNs, Graph Neural Simulators (GNS) have been proposed as powerful data-driven surrogates for time-dependent physical systems [28, 29]. For completeness, a schematic of the GNS architecture, adapted from [28], is presented in Fig. 2. By leveraging message passing [30] to encode local temporal updates, GNS models excel in capturing the evolution of PDE-governed systems on irregular domains, particularly in settings with unstructured meshes, particle-based discretizations, or evolving geometries. This locality-driven formulation enables improved generalization across domains, a challenge where NOs often struggle. Unlike NOs that directly learn global solution operators across function spaces, GNS emphasizes local dynamics by propagating information through graph neighborhoods, offering a more physically intuitive representation. Thus, neural operators and GNN-based simulators represent two complementary paradigms — global operator learning versus local dynamics learning, each with distinct strengths and limitations for modeling complex physical phenomena.

Building on recent work that introduced a DeepONet-based surrogate model for accurate temporal extrapolation in time-dependent PDEs [31], we employ a GNS framework that learns to approximate the instantaneous time derivative of autonomous PDE systems (see Fig. 2). By reformulating the temporal evolution problem as learning the right-hand side (RHS) function, our approach leverages the inherent spatial locality of GNS architectures to model derivative terms while enabling stable long-term integration through established numerical time-stepping schemes. This methodology

combines the geometric flexibility of graph-based representations with the temporal stability of classical numerical methods. In this regard, we make the following key contributions:

- We develop a GNS-based surrogate that serves as an accurate and reliable forward simulator for time-dependent PDEs by learning to model time-derivative fields.
- We rigorously evaluate the generalization performance of the proposed GNS model against the popular NO-based surrogate baselines in the challenging regime of limited training data.
- We introduce a systematic training sample selection strategy (specifically for low data regime) that combines principal component analysis (PCA) [32] with KMeans clustering [33] to ensure sufficient representation of the full dataset through the selected training samples, demonstrating improved performance over pure random sampling approaches.

The remainder of the paper is organized as follows. Section 2 begins with an introduction to graphs in Subsection 2.1, explaining how these data structures provide a more natural representation of physical systems. We then present the mathematical background of the message-passing mechanism in Subsection 2.2, which forms the foundation of all GNN architectures. Building on this foundation, Subsection 2.3 details the complete GNS architecture, followed by Subsection 2.4, which describes how we leverage GNS to construct accurate forward models for PDE systems. Finally, we present comprehensive experimental results in Section 3, summarize our findings in Section 4, and outline limitations and future research directions in Section 5.

## 2 Graph Neural Networks (GNNs)

Graphs provide a flexible and expressive data structure for representing spatial relationships and interactions in non-Euclidean domains [34, 35]. By non-Euclidean data, we refer to data that cannot be conveniently embedded into regular, uniformly spaced grids such as those used in standard image processing. Instead, the physical domain is denoted using irregular meshes where connectivity between points is determined by physical relationships, topology, solution gradient or geometry rather than fixed spatial coordinates. In the following subsections, we outline the motivation for using graphs as an alternative data structure, define key terminologies, introduce the mathematical background of message passing, present a thorough overview of Graph Neural Simulators including their encoder, processor, and decoder components, and finally demonstrate how GNS can be leveraged to build accurate, reliable, and stable surrogate models for solving time-dependent PDE systems.

### 2.1 Graphs

A graph  $G = (\mathcal{V}, \mathcal{E})$  broadly consists of two entities:

1. Vertices (nodes):  $\mathbf{v}_i \in \mathcal{V}$ , representing individual elements in the system - such as mesh nodes or particles. Each node can store features describing its physical state (e.g., velocity, pressure, position, temperature).
2. Edges:  $\mathbf{e}_{ij} \in \mathcal{E}$  represent relationships or interactions between node pairs  $\mathbf{v}_i$  and  $\mathbf{v}_j$ . Edges may be defined by mesh connectivity, spatial proximity (e.g.,  $k$ -nearest neighbors), or physical constraints, and can store edge features such as relative distances, relative velocities, or interaction coefficients. They may be either directed or undirected, depending on the flow of information between the two nodes of interest.

Graphs offer a *permutation-invariant* representation of data, meaning that the interaction between nodes is independent of their ordering or their absolute positions in the Euclidean space. Furthermore, since graphs encode interactions between any two nodes via edge connections, the *relative* positional information between nodes is often sufficient to model such interactions, rather than requiring absolute coordinates. As a result, graphs provide an efficient and physically consistent framework for modeling interaction behavior in a wide range of systems, particularly those where local or pairwise relationships dictate the dynamics.

In GNNs, learning over the constructed graph is typically performed through a *message-passing* mechanism [30]. At each iteration (or layer), nodes exchange information with their neighbors via the edges, aggregating the incoming messages to update their own states. This paradigm naturally

captures local interactions, long-range dependencies through multiple hops, and physical invariances such as translational and rotational symmetry. Formally, a GNN takes a graph  $G = (\mathcal{V}, \mathcal{E})$  as input, computes the interaction behavior by iteratively updating the properties of its nodes and edges, and returns an updated graph  $G' = (\mathcal{V}', \mathcal{E}')$ , where the connectivity structure remains unchanged but the node features  $\mathbf{v}'_i$  and edge features  $\mathbf{e}'_{i,j}$  are updated.

## 2.2 Message Passing on Graphs

As mentioned previously, the interaction dynamics between the nodes of a graph are learned through message passing, which provides a principled way of updating node and (optionally) edge feature vectors by incorporating the influence of both immediate and multi-hop neighbors. A single message-passing step generally consists of three stages:

1. Message Construction:

$$\mathbf{e}'_{i,j} = \mathbf{m}_{i,j} = f_\theta(\mathbf{v}_i, \mathbf{v}_j, \mathbf{e}_{i,j}).$$

2. Message Aggregation (e.g., sum):

$$\bar{\mathbf{v}}_i = \sum_{j \in \mathcal{N}(i)} \mathbf{e}'_{i,j}.$$

3. Node Update:

$$\mathbf{v}'_i = f_\phi(\mathbf{v}_i, \bar{\mathbf{v}}_i).$$

Here,  $f_\theta$  and  $f_\phi$  are functions (typically neural networks) with learnable parameters  $\theta$  and  $\phi$ , respectively. The aggregation operator,  $\bar{\mathbf{v}}_i$ , can be any permutation-invariant function (e.g., sum, mean, max), ensuring that the result is independent of the ordering of neighbors.

In the message construction step,  $f_\theta$  takes as input the concatenated feature vectors of the sender node  $\mathbf{v}_j$ , the receiver node  $\mathbf{v}_i$ , and the edge connecting them  $\mathbf{e}_{i,j}$ , producing an updated edge feature vector  $\mathbf{e}'_{i,j}$ , also referred to as the message  $\mathbf{m}_{i,j}$ . This operation is performed for all neighbors  $j \in \mathcal{N}(i)$  of the target (receiver) node  $i$ . Next, in the message aggregation step, all incoming messages  $\mathbf{e}'_{i,j}$  from the neighbors of node  $i$  are combined via a permutation-invariant aggregation function to produce an aggregated message vector  $\bar{\mathbf{v}}_i$ . Finally, in the node update step,  $f_\phi$  takes both the current feature vector  $\mathbf{v}_i$  and the aggregated message  $\bar{\mathbf{v}}_i$  to produce the updated node feature vector  $\mathbf{v}'_i$ .

At the end of one message-passing step (or one GNN layer), the node and edge features  $(\mathbf{v}_i, \mathbf{e}_{i,j})$  are updated to  $(\mathbf{v}'_i, \mathbf{e}'_{i,j})$  based on the 1-hop neighborhood. To capture information from more distant nodes (i.e.,  $k$ -hop neighbors with  $k > 1$ ), multiple message-passing steps are applied sequentially, allowing the influence of far-reaching interactions to propagate through the graph. Building on the concept of message passing, in the next section we discuss a widely adopted GNN-based architecture for simulating complex physical dynamics: the *Graph Neural Simulator* (GNS) [28, 29].

## 2.3 Graph Neural Simulators (GNS)

At a high level, the GNS framework uses a GNN as the backbone with three main components: (1) Encoder, (2) Processor, and (3) Decoder. The encoder takes the physical state of the system and embeds it into a graph representation by defining nodes according to a chosen connectivity rule and assigning node features that represent physical quantities (e.g., position, velocity, or material properties). These features are then mapped into a latent space via learnable transformations. The processor performs multiple rounds of message passing to update the latent node features, propagating information across the graph and capturing both local and long-range interactions. The decoder takes the updated graph representation and projects the latent features back into the physical space to produce dynamic quantities of interest, such as velocities or accelerations at each node. In the following sections, we describe each of these components in detail along with the creation of inputs to the GNS.

1. **Encoder:** The encoder maps the physical state of the system into a latent graph representation suitable for message passing. Formally, let the physical system be represented as a graph  $G = (\mathcal{V}, \mathcal{E})$ , where  $\mathcal{V} = \{1, \dots, N\}$  denotes the set of nodes (e.g., grid points, particles) and  $\mathcal{E} \subseteq \mathcal{V} \times \mathcal{V}$  denotes the set of edges defined according to a chosen connectivity rule. Note that the edges can be both directed or undirected.

In structured mesh-based domains, the grid naturally forms a graph with each grid point serving as a node. The edges follow standard finite-difference stencils, such as 4-nearest or 8-nearest neighbors in two-dimensional meshes. For unstructured or irregular domains, connectivity is often determined by a radius-based rule: an edge  $(i, j)$  is created if  $\|\mathbf{x}_i - \mathbf{x}_j\|_2 \leq r_c$ , where  $r_c$  is a predefined connectivity radius. Alternatively,  $k$ -nearest neighbor graphs are used, where each node  $i$  is connected to its  $k$  closest nodes in Euclidean space. Each node  $i \in \mathcal{V}$  is associated with a feature vector  $\mathbf{v}_i^{(0)} \in \mathbb{R}^{d_v}$ , which may include physical quantities of interest (e.g., velocity, temperature), static material properties (e.g., density, elasticity), positional coordinates  $\mathbf{x}_i \in \mathbb{R}^d$ , and boundary condition flags or positional encodings. Similarly, each edge  $(i, j) \in \mathcal{E}$  has a feature vector  $\mathbf{e}_{i,j}^{(0)} \in \mathbb{R}^{d_e}$ , which can encode relative displacement  $\mathbf{x}_j - \mathbf{x}_i$ , Euclidean distance  $\|\mathbf{x}_j - \mathbf{x}_i\|_2$ , or material-specific interaction parameters.

The encoder transforms these raw features into a latent representation through learnable mappings:

$$\mathbf{h}_i^{(0)} = \hat{f}_{\text{node}}(\mathbf{v}_i^{(0)}), \quad \mathbf{z}_{i,j}^{(0)} = \hat{f}_{\text{edge}}(\mathbf{e}_{i,j}^{(0)}),$$

where  $\hat{f}_{\text{node}}$  and  $\hat{f}_{\text{edge}}$  are typically neural networks with trainable parameters. Here, the subscripts  $i$  and  $j$  denote node indices, while the superscript  $(0)$  indicates the initial layer (pre-processing stage). The resulting latent graph  $(\{\mathbf{h}_i^{(0)}\}, \{\mathbf{z}_{i,j}^{(0)}\})$  serves as input to the *Processor* stage, which performs the message passing operations.

2. **Processor:** The processor is the core computational module of the GNS, responsible for propagating information across the graph through multiple rounds of message passing. Given the latent graph from the encoder,  $(\{\mathbf{h}_i^{(0)}\}, \{\mathbf{z}_{i,j}^{(0)}\})$ , the processor updates node and edge features iteratively over  $L$  message-passing layers. In each layer  $\ell = 0, 1, \dots, L-1$ , messages are first constructed for every edge  $(i, j) \in \mathcal{E}$  as

$$\mathbf{m}_{i,j}^{(\ell)} = f_\theta(\mathbf{h}_i^{(\ell)}, \mathbf{h}_j^{(\ell)}, \mathbf{z}_{i,j}^{(\ell)}),$$

where  $f_\theta$  is a neural network with learnable parameters  $\theta$  that generates messages based on connected node features and edge attributes. These messages are then aggregated at each receiving node  $i$  using a permutation-invariant operator:

$$\bar{\mathbf{m}}_i^{(\ell)} = \text{AGG}(\{\mathbf{m}_{i,j}^{(\ell)} : j \in \mathcal{N}(i)\}),$$

where  $\mathcal{N}(i)$  denotes the set of neighbors of node  $i$ , and AGG may be a sum, mean, or max operation. The aggregated message is then used to update the node features via a separate node update function:

$$\mathbf{h}_i^{(\ell+1)} = f_\phi(\mathbf{h}_i^{(\ell)}, \bar{\mathbf{m}}_i^{(\ell)}),$$

where  $f_\phi$  is another neural network with learnable parameters  $\phi$  that combines the current node state with incoming messages. Note that  $\theta$  and  $\phi$  represent different sets of trainable parameters for the message generation and node update functions, respectively, allowing each component to learn independent specialized transformations.

If edge features are also updated, a learnable edge update function with parameters  $\psi$ :

$$\mathbf{z}_{i,j}^{(\ell+1)} = f_\psi(\mathbf{h}_i^{(\ell)}, \mathbf{h}_j^{(\ell)}, \mathbf{z}_{i,j}^{(\ell)})$$

can be applied in parallel. After  $L$  such layers, the processor outputs the updated latent graph  $(\{\mathbf{h}_i^{(L)}\}, \{\mathbf{z}_{i,j}^{(L)}\})$ , which encodes both local and long-range interactions.

3. **Decoder:** The decoder maps the processed latent graph representation back to the physical space to produce the target quantities of interest. Given the final node embeddings  $\{\mathbf{h}_i^{(L)}\}$  from the processor, the decoder applies a learnable mapping

$$\mathbf{y}_i = g_\omega(\mathbf{h}_i^{(L)}),$$

where  $g_\omega$  is a neural network with parameters  $\omega$ , and  $\mathbf{y}_i \in \mathbb{R}^{d_y}$  represents the predicted physical quantities at node  $i$  (e.g., velocity, acceleration, pressure). When the task requires edge-level predictions, an analogous mapping

$$\mathbf{y}_{i,j} = g_\eta(\mathbf{z}_{i,j}^{(L)})$$

can be applied to the final edge embeddings. The decoder thus produces simulation outputs in the desired physical space, completing the encoder–processor–decoder pipeline of the GNS architecture.

## 2.4 GNS as a forward simulator for PDEs

Consider a general time-dependent PDE system governing the evolution of a spatiotemporal field  $u(\mathbf{x}, t)$ , defined over a temporal domain  $t \in [0, T]$  and a spatial domain  $\mathbf{x} = [x_1, x_2, \dots, x_n]$ , with  $\mathbf{x} \in \mathcal{X} \subseteq \mathbb{R}^n$ . The dynamics of this system can be expressed as

$$\frac{\partial u}{\partial t} = \mathcal{G}(t, \mathbf{x}, u, u_{\mathbf{x}}, u_{\mathbf{xx}}, u_{\mathbf{xxx}}, \dots), \quad (1)$$

where  $\mathcal{G}$  denotes the PDE operator relating the temporal derivative of the field to its spatial derivatives.

As discussed previously, recent work [31] introduced a DeepONet-based surrogate model for solving time-dependent PDEs by reformulating the operator learning task to predict instantaneous time-derivative fields conditioned on the current system state. This is equivalent to learning a parametric approximation  $\mathcal{G} \approx \mathcal{G}_\theta$  for the right-hand side of the PDE. Inspired by this formulation, we adopt a GNS framework to model the time derivative. The motivation is that GNS architectures inherently capture spatial interactions between discretization points, making them well-suited for approximating the spatial derivative terms appearing in  $\mathcal{G}$ . In this work, we focus on *autonomous systems*, where the right-hand side does not explicitly depend on time.

Once trained to approximate the instantaneous time derivative, the GNS can be integrated forward in time using any stable numerical time-stepping method. For instance, with the explicit Euler scheme, a one-step update from state  $u^t$  to  $u^{t+1}$  is given by

$$u^{t+1} = u^t + \Delta t \cdot \text{GNS}(u^t), \quad (2)$$

where  $\Delta t$  is the time step size. At inference time, the solution can be evolved from an initial condition by repeatedly applying the numerical scheme using the GNS-predicted time derivative. In this way, the GNS effectively serves as a forward simulator for the PDE system. Note that while we employ the first-order explicit Euler scheme, the same formulation holds for any higher-order numerical integration scheme.

Graph construction, along with the definition of appropriate node and edge feature vectors, forms the fundamental first step in the GNN learning process. In this work, we construct the graph by treating spatial grid points in the domain as nodes. For instance, in a two-dimensional grid, each node corresponds to a spatial location  $x_{(i,j)} \in \mathbb{R}^2$  where  $i \in \{1, 2, \dots, N_x\}$  and  $j \in \{1, 2, \dots, N_y\}$ , such that the total number of nodes is  $N = N_x \times N_y$ . To define edge connectivity, we employ a finite-difference-like stencil and connect each node to its  $k$ -nearest neighbors, with  $k = 8$  in our case. Therefore, a target node's neighborhood includes the left, right, top, bottom, and four diagonal neighbors. The edge set is thus defined as  $\mathcal{E} = \{(u, v) \mid v \in \mathcal{N}_k(u)\}$ , where  $\mathcal{N}_k(u)$  refers to the  $k$ -nearest neighboring nodes of target node  $u$ .

To reiterate, while solving physical systems using GNNs, it is imperative to assign a node feature vector that captures both the physical fields and the geometric embedding of the node. Specifically, in this work, the node features include: (i) the physical field values of interest at the node (*e.g.*, velocity, pressure, or material parameters), (ii) the absolute positional coordinates  $(x_u, y_u)$ , and (iii) Fourier positional encodings of the form  $[\sin(\omega x_u), \cos(\omega x_u), \sin(\omega y_u), \cos(\omega y_u)]$ . The idea behind including additional static node features, *i.e.*, features that are not updated at every message-passing step (*e.g.*, Fourier embeddings in this case), is to provide a richer context and enhance the representation capacity by embedding the spatial coordinates into a better feature space, thereby improving the learning process. The edge feature vectors between any pair of connected nodes  $(u, v) \in \mathcal{E}$  are designed to encode both (relative) geometric information and physical interactions. For our work, we consider an edge feature vector that includes the following quantities:

1. Relative displacement vector between the target node  $u$  and sender node  $v$ :  $\Delta \mathbf{x}_{(u,v)} = \mathbf{x}_v - \mathbf{x}_u$
2. Euclidean distance between the nodes  $u$  and  $v$ :  $d_{(u,v)} = \|\Delta \mathbf{x}_{(u,v)}\|_2$
3. Difference in the physical fields between the two nodes:  $\Delta f_{(u,v)} = f_v - f_u$
4. Norm of the difference in physical fields between the two nodes:  $\|\Delta f_{(u,v)}\|_2$

## 3 Results

The key objective of this study is to evaluate the generalization capabilities of GNS-based surrogate models in comparison with neural operator (NO)-based surrogates. We focus on representative

examples from two broad classes of NOs: (1) universal approximation theorem-based methods (*e.g.*, deep operator networks (DeepONet)) and (2) kernel integral operator-based methods (*e.g.*, Fourier Neural Operators (FNO)). Specifically, we examine four DeepONet-based and two FNO-based frameworks: (1) DeepONet Full Rollout (DON-FR), (2) DeepONet Autoregressive (DON-AR), (3) Time-Integrated DeepONet (TI-DON), (4) Time-Integrated DeepONet with Learned Integration (TI(L)-DON), (5) FNO Full Rollout (FNO-FR), and (6) FNO Autoregressive (FNO-AR). For brevity, we do not present the architectural details of all the neural operators and their variants. A detailed discussion and a comparative study of these NO-based models can be found in [31].

To ensure a fair and comprehensive evaluation, we benchmark both GNS and NO frameworks on four canonical PDE systems that cover a diverse range of complex, nonlinear, high-dimensional, and spatiotemporal dynamics: (1) the 2D Burgers' equation with a scalar field solution, (2) the 2D coupled Burgers' equation with a vector field solution, (3) the 2D Allen–Cahn equation, and (4) the 2D nonlinear shallow water equations (SWE). Since we are comparatively assessing the generalization performance of the GNS surrogate against other NO baselines for time-dependent PDEs, we restrict our study to uniform grids, as most NO architectures (*e.g.*, FNO) require a uniform grid domain. For the comparison of inference errors, we consider a relative  $L_2$  error metric, defined as

$$\varepsilon_{L_2} = \frac{\|u_{\text{pred}} - u_{\text{truth}}\|_2}{\|u_{\text{truth}}\|_2}, \quad (3)$$

where  $u_{\text{pred}}$  and  $u_{\text{truth}}$  denote the predicted and ground truth solutions, respectively.

Figure 3 depicts the temporal error accumulation observed across all frameworks and the first three PDE examples considered in this study. Across these PDE systems, GNS (black) consistently exhibits the lowest error growth with a noticeable plateauing of errors, indicating that the GNS surrogate demonstrates accurate, reliable, and stable performance over extended temporal horizons. This is followed by FNO-FR (blue) and FNO-AR (orange), with FNO-FR performing better than FNO-AR for longer timesteps except in the 2D Burgers' scalar case, where FNO-AR surpasses FNO-FR beyond  $t = 0.7$ . Note that FNO-FR incurs appreciable errors for the initial few timesteps across all three cases, beyond which it outperforms FNO-AR. Finally, DeepONet-based frameworks incur substantially higher errors than their counterparts, *i.e.*, FNO and GNS. The primary reason is that DeepONet generally requires significantly more training data than the other methods to construct an accurate set of basis functions and coefficients. Among the DeepONet frameworks, the time-integrator variants, TI(L)-DON (magenta) and TI-DON (green), perform better than DON-FR (red) for the initial timesteps until  $t = 0.45$  or  $t = 0.5$ . Beyond this point, DON-FR surpasses these frameworks. The aforementioned observations translate directly to the comparison plots in subsequent sections where we discuss individual cases separately and examine this phenomenon through both qualitative and quantitative assessment of generalization performance via relative  $L_2$  test errors during inference. Details regarding the computational costs incurred during training and inference are provided in Table A1 in the Supplementary Information (SI). Additional information on the network architectures, as well as further results on predicted solution contours, is provided in SI B and SI C, respectively. The code to reproduce the experiments is publicly available at [https://github.com/Centrum-IntelliPhysics/GNS\\_vs\\_NOs.git](https://github.com/Centrum-IntelliPhysics/GNS_vs_NOs.git).

### 3.1 Two-Dimensional Burgers' Equation with Scalar Output Field

In the first example, we consider the two-dimensional viscous Burgers' equation with a scalar output field. This PDE, often regarded as a simplified form of the Navier–Stokes equations, captures essential features of fluid transport by balancing nonlinear advection with viscous diffusion. Despite its relative simplicity, it exhibits rich spatiotemporal dynamics and is widely used as a benchmark for surrogate modeling. The governing equation is:

$$\frac{\partial u}{\partial t} + u \frac{\partial u}{\partial x} + u \frac{\partial u}{\partial y} = \nu \left( \frac{\partial^2 u}{\partial x^2} + \frac{\partial^2 u}{\partial y^2} \right), \quad \forall (x, y, t) \in [0, 1]^2 \times [0, 1], \quad (4)$$

where  $u(x, y, t)$  is a scalar field and  $\nu = 0.01$  is the kinematic viscosity. The IC,  $u(x, y, 0) = u_0(x, y)$  is sampled from 2D Gaussian random field, and periodic Dirichlet and Neumann BCs are applied in both  $x$  and  $y$  directions.

Mathematically, this is a nonlinear parabolic PDE in which convective terms steepen the gradients while diffusion smoothens them, leading to phenomena such as viscous shock formation and spatiotemporal mixing. For surrogate modeling, two challenges arise: (i) the nonlinearity amplifies

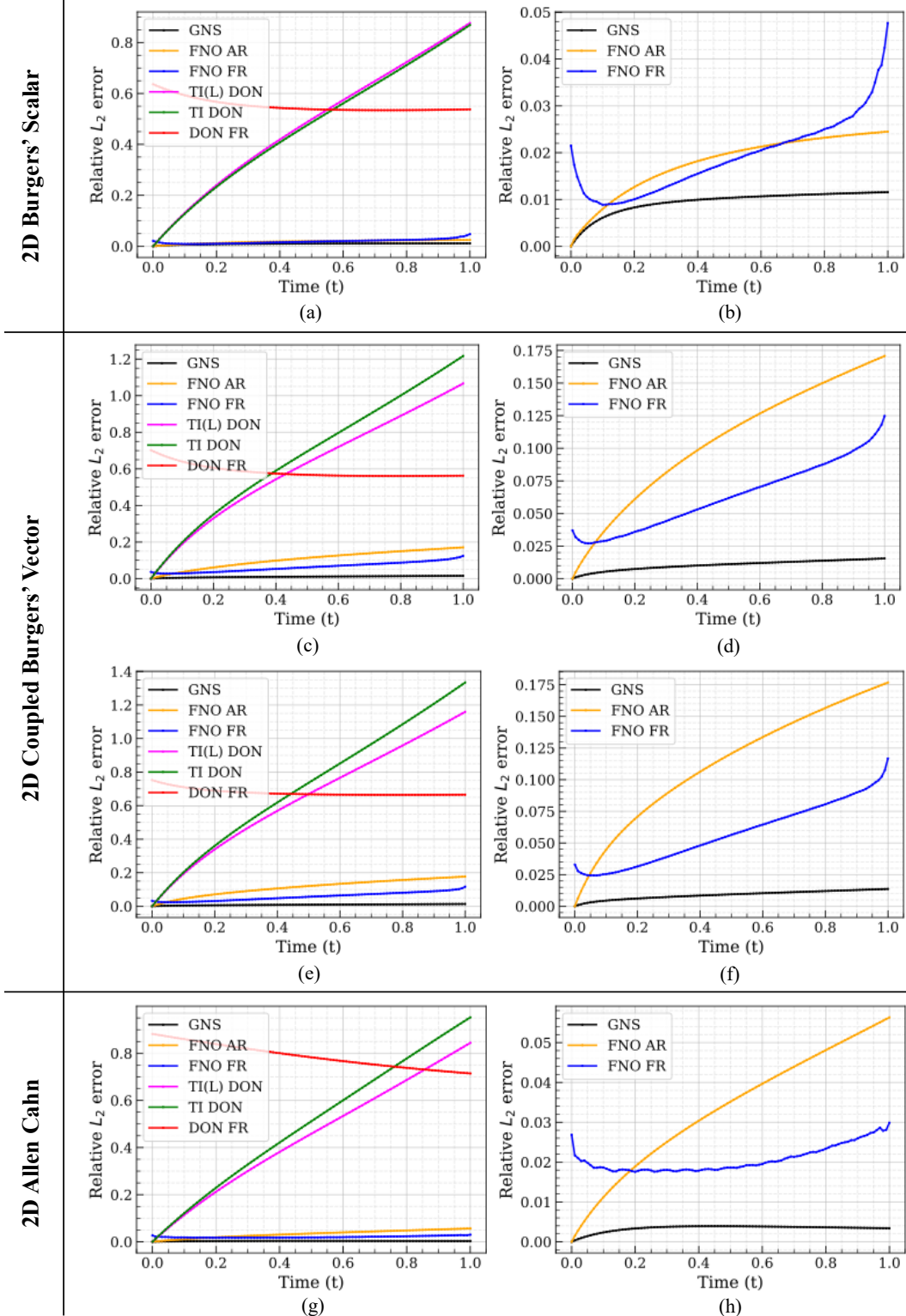


Figure 3: Temporal evolution of error accumulation across different frameworks for the 2D Burgers' scalar, 2D Burgers' vector, and 2D Allen-Cahn examples, trained with 30 trajectories. Left: comparison of all NO baselines with the GNS surrogate model. Right: comparison of the GNS surrogate model with the FNO variants (FNO-FR and FNO-AR). In the 2D coupled Burgers' case, figures (c) and (d) correspond to the  $u$ -velocity field, while figures (e) and (f) correspond to the  $v$ -velocity field.

Table 1: Ground truth dataset generation details for the four PDE cases. The data generation script for the 2D Burgers' examples and the 2D nonlinear SWE example was adapted from [36]. The generalization error of all frameworks for each PDE is evaluated using training data sizes of 30, 50, 70, and 100 samples. Training trajectories are selected using a combined PCA and KMeans approach.

Case	GRF Kind	BCs	$l$	$\sigma$	$N_s$	$N_{train}$	$N_{test}$	$N_x \times N_y$	$N_t$
2D Burgers' Scalar	Matérn	Periodic	0.125	0.15	1000	30	1000	$32 \times 32$	101
						50			
						70			
						100			
2D Burgers' Vector	Matérn	Periodic	0.1	0.2	500	30	500	$64 \times 64$	101
						50			
						70			
						100			
2D Allen-Cahn	Squared-Exponential	Periodic	0.05	Normalized to [-1,1]	1000	30	1000	$32 \times 32$	101
						50			
						70			
						100			
2D nonlinear SWE	Matérn	Periodic	0.1	0.2	500	30	500	$64 \times 64$	101
						50			
						70			
						100			

approximation errors during long-horizon rollouts, and (ii) the relative influence of convection and diffusion, controlled by  $\nu$ , requires the model to generalize across regimes ranging from diffusion-dominated to advection-dominated dynamics.

To select training trajectories, we adopt a strategy combining principal component analysis (PCA) with KMeans clustering. Specifically, the full dataset is projected onto its first 20 principal components, after which KMeans clustering is performed with the number of clusters equal to the desired number of training trajectories. From each cluster, we then select the trajectory closest to the centroid in terms of Euclidean distance. This procedure ensures that the chosen training set captures the diversity of the full dataset in a more systematic manner than pure random sampling. While many sophisticated sampling strategies exist in the literature, we employ this relatively simple yet intuitive approach as a principled way of trajectory selection.

We next provide a brief description of the learning strategies employed by the various frameworks. GNS learns a one-timestep mapping  $u_t \rightarrow u_{t+1}$  by estimating the time derivative conditioned on the current state,  $\frac{\partial u}{\partial t} \big|_{u(t,x,y)}$ , and then applies an explicit Euler update to predict the next state  $u(t+1, x, y)$  from the input state  $u(t, x, y)$ . The full rollout methods, such as FNO-FR and DON-FR, learn the solution operator that maps the initial condition to the entire spatiotemporal output field, *i.e.*,  $\mathcal{G} \sim \mathcal{G}_\theta : u_0(x, y) \rightarrow u(t, x, y)$ . In contrast, the autoregressive frameworks, such as FNO-AR and DON-AR, directly learn the one-timestep mapping operator that advances the solution state forward in time, *i.e.*,  $\mathcal{G} \sim \mathcal{G}_\theta : u(t, x, y) \rightarrow u(t+1, x, y)$ . Finally, the time integrator (TI)-based frameworks (see [31] for more details) learn the instantaneous time-derivative operator, *i.e.*,  $\mathcal{G} \sim \mathcal{G}_\theta : u(t, x, y) \rightarrow \frac{\partial u}{\partial t} \big|_{u(t,x,y)}$ . It is noteworthy that the learning strategies of GNS and the TI-based frameworks are analogous, with the latter having more relevance in an operator learning setting.

Figure 4 presents a comparison of the absolute error in predictions for a representative test trajectory across all frameworks. Among the DeepONet-based models, the autoregressive variant (DON-AR) incurs errors nearly an order of magnitude higher than the others. This can be attributed to its greater sensitivity to error accumulation during inference and the limited generalization ability of DeepONet in data-scarce regimes. The full rollout DeepONet (DON-FR) and the time-integrator (TI)-based variants yield comparable errors, with DON-FR performing qualitatively worse than the TI-based frameworks during the early timesteps ( $t = \{0.2, 0.4, 0.5\}$ ). Between the TI-based

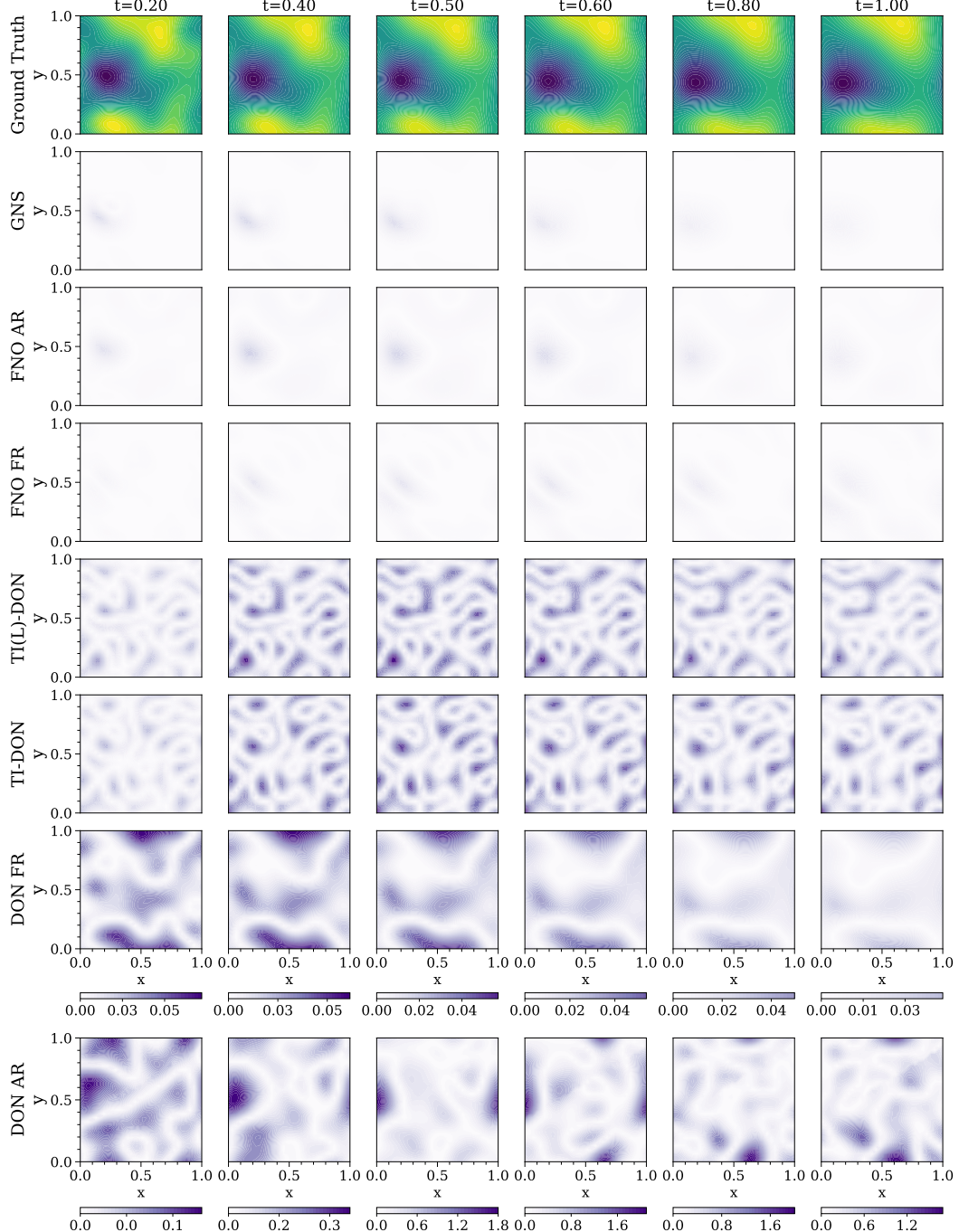


Figure 4: 2D Burgers' equation with scalar output field. Performance of all frameworks trained on 30 trajectories and evaluated on 1000. Top row: ground truth solution contours; subsequent rows: absolute error contours for each framework.

models, the learnable version, TI(L)-DeepONet, consistently outperforms its vanilla counterpart, *i.e.*, TI-DeepONet. In contrast, the Fourier Neural Operator (FNO)-based frameworks demonstrate markedly better performance. Both the full rollout (FNO-FR, using FNO-3D) and autoregressive (FNO-AR, using FNO-2D) variants achieve lower prediction errors than all DeepONet-based models, with errors marginally below those of the GNS. Finally, GNS achieves the best overall performance,

significantly reducing generalization error and producing predictions that closely match the ground truth contours, even when trained on only 30 trajectories. This superior accuracy can be attributed to the strong inductive bias encoded in the GNS architecture: by explicitly modeling local spatial interactions between nodes in the computational graph, GNS effectively mirrors the underlying physical dynamics, thereby enabling robust learning in data-scarce regimes.

Table 2: Two-Dimensional Burgers’ equation with scalar output field: Inference errors for  $u$  fields across different methods and training trajectory counts. At inference, 1000 trajectories are used, with a timestep of  $\Delta t = 0.01$  for the time-integrator-based frameworks (GNS, TI-DON, TI(L)-DON).

Method	Training Trajectories			
	30	50	70	100
GNS	<b>0.0088</b>	<b>0.0045</b>	<b>0.00386</b>	<b>0.003626</b>
DON FR	0.56441	0.2892	0.20913	0.13424
DON AR	6.69263	6.55041	3.3983	1.16416
TI-DON	0.430894	0.29132	0.20473	0.17639
TI(L)-DON	0.43951	0.28119	0.2067	0.17559
FNO AR	0.01636	0.012934	0.006145	0.005266
FNO FR	0.017577	0.013386	0.010369	0.006383

Next, we quantitatively assess the generalization performance of all frameworks by computing the overall relative  $L_2$  test error on 1000 unseen trajectories, with models trained on subsets of 30, 50, 70, and 100 trajectories. The summarized results are reported in Table 2. These observations are consistent with the qualitative comparisons presented in Figure 4. As expected, increasing the number of training trajectories reduces inference error across all frameworks, consistent with the well-established fact that larger training datasets help narrow the generalization gap in data-driven models. Among the DeepONet-based frameworks, DON-AR consistently exhibits the largest relative  $L_2$  errors, nearly an order of magnitude higher than all other methods, confirming its larger sensitivity to error accumulation during rollout. This is followed by DON-FR, TI-DON, and TI(L)-DON. For smaller training sets (30 and 50 trajectories), TI(L)-DON outperforms TI-DON and DON-FR, likely due to its ability to learn adaptive integration weights. At 70 training trajectories, these three methods perform comparably, while with 100 training trajectories, DON-FR slightly surpasses the TI-based variants. This improvement can be attributed to DON-FR’s more accurate basis functions and coefficients representative of the output function space, which better captures the PDE dynamics at higher data availability.

In contrast, the FNO-based frameworks (FNO-FR and FNO-AR) perform significantly better than their DeepONet counterparts. This can be attributed to two main reasons. First, DeepONet operates in physical space and being based on the universal approximation theorem for operators, is inherently more data-hungry. Second, learning the solution operator in spectral space provides a distinct advantage: for dissipative systems such as Burgers’, FNO captures global features (dominant modes) in the spatiotemporal solution, resulting in stronger generalization capacity. While FNO is itself data-hungry, the dynamics of the Burgers’ PDE favors spectral learning, thereby enhancing its performance.

Finally, the GNS framework outperforms all other methods by a substantial margin. Remarkably, GNS achieves a relative  $L_2$  error as low as 0.88% when trained on only 30 trajectories. This superior performance aligns with our earlier analysis: by explicitly modeling spatial interactions through its graph-based architecture, GNS embeds a strong physics-aware inductive bias, allowing it to naturally encode the underlying dynamical laws of the system and generalize robustly even in the data-scarce regime.

### 3.2 Two-Dimensional Coupled Burgers’ Equation with Vector Output Field

The second example we consider is the two-dimensional coupled Burgers’ equation with vector-valued outputs, representing the velocity components  $u(x, y, t)$  and  $v(x, y, t)$ . This system can be regarded as a simplification of the incompressible Navier–Stokes equations that does not account

for pressure effects, extending the scalar Burgers' equation by introducing two interacting velocity fields. In doing so, it captures richer transport phenomena by balancing nonlinear cross-advection with viscous diffusion. The system is defined on the spatial domain  $(x, y) \in [0, 1]^2$  over the time interval  $t \in [0, 1]$ , and its governing equations are:

$$\frac{\partial u}{\partial t} + u \frac{\partial u}{\partial x} + v \frac{\partial u}{\partial y} = \mu \left( \frac{\partial^2 u}{\partial x^2} + \frac{\partial^2 u}{\partial y^2} \right), \quad (5)$$

$$\frac{\partial v}{\partial t} + u \frac{\partial v}{\partial x} + v \frac{\partial v}{\partial y} = \mu \left( \frac{\partial^2 v}{\partial x^2} + \frac{\partial^2 v}{\partial y^2} \right), \quad (6)$$

where  $\mu = 0.01$  denotes the viscosity coefficient. The initial conditions  $u(x, y, 0) = u_0(x, y)$  and  $v(x, y, 0) = v_0(x, y)$  are sampled from two-dimensional Gaussian random fields, while periodic Dirichlet and Neumann boundary conditions are imposed in both  $x$  and  $y$  directions.

Mathematically, this system is a nonlinear parabolic PDE with coupled advection–diffusion dynamics. The convective terms jointly transport both velocity components, while the viscous terms act to dissipate energy and smooth the solution. Physically, this makes the system a closer analog to the Navier–Stokes equations, albeit without the pressure term and incompressibility constraint. The coupling between  $u$  and  $v$  gives rise to complex spatiotemporal structures, including interacting shear layers and vortex-like features, which are absent in the scalar case. From a surrogate modeling perspective, additional challenges arise due to (i) the cross-advection terms, which tightly couple the dynamics of  $u$  and  $v$ , and (ii) the increased dimensionality of the output field, requiring the model to simultaneously learn and generalize across both velocity components. Compared to the scalar case, this coupled vector formulation represents a more challenging benchmark for evaluating the generalization capabilities of all the surrogate models considered in this study. The ground truth dataset is generated following a similar approach as the previous case, where the initial conditions  $u_0(x, y)$  and  $v_0(x, y)$  are sampled from periodic Matérn-type Gaussian random fields (GRFs) (see Table 1 for specific details). For training trajectory selection, we employ the PCA-KMeans procedure described in Section 3.1, retaining the first 50 principal components during the PCA dimensionality reduction step.

In a similar spirit, we first present a qualitative comparison of the prediction test errors incurred during inference on 1000 trajectories, trained on 30 trajectories. The results are shown in Figs. 5 and 6 for the  $u$  and  $v$  velocity fields, respectively. While the contours are displayed separately for the two fields, the overall trends remain consistent across both. As before, DON-AR exhibits errors an order of magnitude larger than all other methods, which can be attributed to its high sensitivity to error accumulation, exacerbated by the limited availability of training data. Among the other DeepONet-based variants, the TI-based frameworks (TI(L)-DON and TI-DON) outperform DON-FR during the initial rollout (up to  $t = 0.4$ ). Beyond this temporal horizon, DON-FR surpasses the TI-based methods and achieves lower test errors. Within the TI family, TI(L)-DON consistently outperforms the vanilla TI-DON due to its ability to adapt to local solution features, an advantage that becomes especially useful when training data is scarce.

In contrast, the FNO-based approaches achieve significantly lower errors than the DeepONet-based methods, with FNO-FR marginally outperforming FNO-AR in this case. This behavior is expected, as the coupled Burgers' PDE is more amenable to learning in spectral space, where dominant frequency modes of the solution dynamics can be effectively captured even with limited data. Nevertheless, it is worth noting that while FNO outperforms DeepONet here, neural operators in general remain data-hungry, and we hypothesize that FNO would require substantially more training data for PDEs with richer frequency spectra. Finally, compared to all operator-learning methods, GNS once again delivers the best performance, achieving an almost perfect match with the ground truth for both the  $u$  and  $v$  velocity fields.

Table 3 summarizes the overall relative  $L_2$  inference errors for predicting the  $u$  and  $v$  velocity fields using 30, 50, 70, and 100 training trajectories. The observed trends align closely with the qualitative comparisons in Figs. 5 and 6. As expected, DON-AR performs the worst, with relative  $L_2$  errors exceeding 100% across all cases, indicating that its predicted solutions deviate entirely from the ground truth. Among the remaining DeepONet-based frameworks, the TI variants (TI-DON and TI(L)-DON) achieve slightly lower errors than DON-FR when trained with only 30 trajectories and perform comparably for 50 and 70 trajectories. However, when sufficient training data is provided, DON-FR yields more accurate basis function and coefficient representations of the output solution space, ultimately surpassing the TI variants in predictive accuracy.

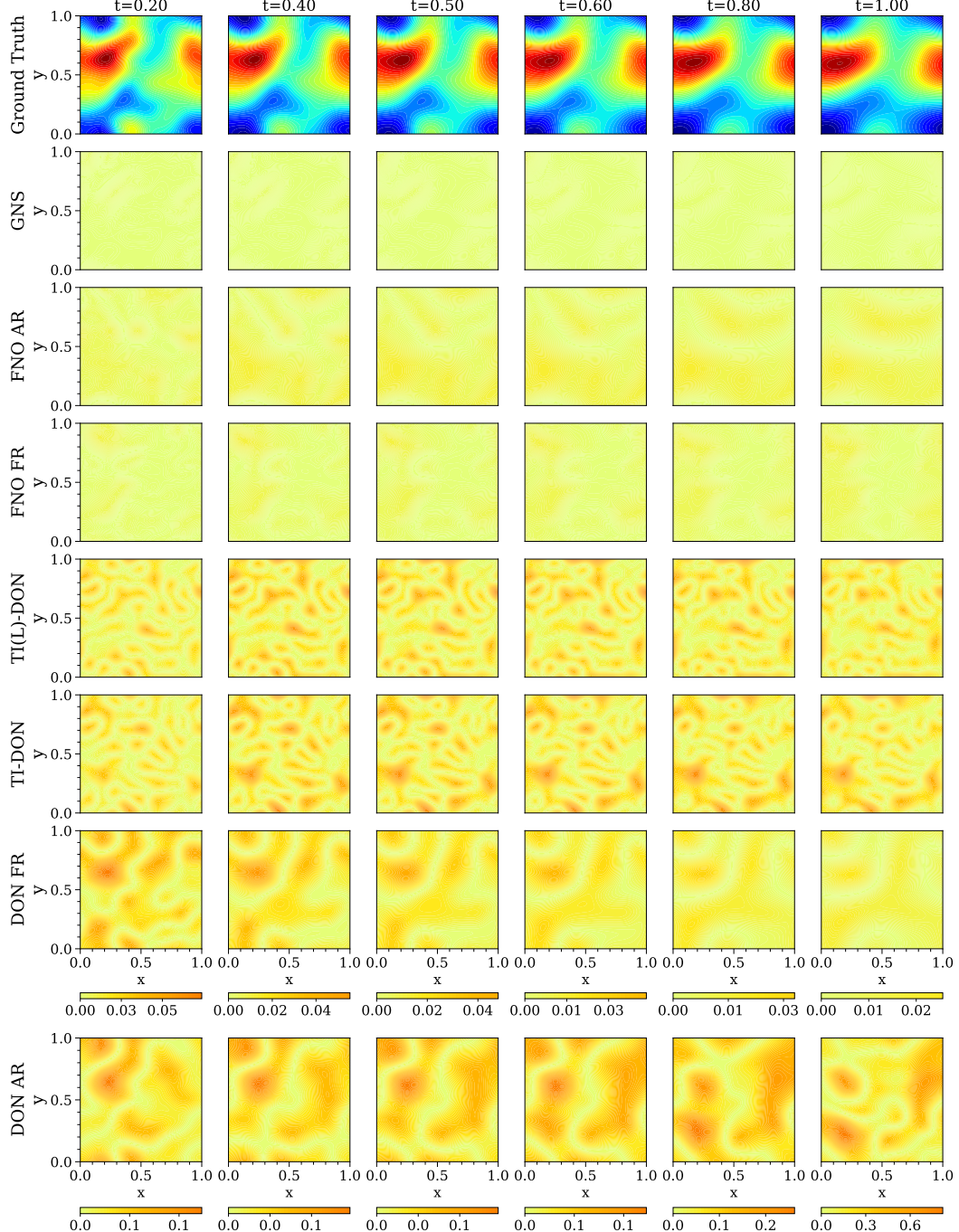


Figure 5: 2D coupled Burgers' equation with a vector output field: Performance of all frameworks on 30 training trajectories, evaluated on 500 trajectories for predicting the  $u$ -velocity field of a representative sample. Top row: ground truth solution contours; subsequent rows: absolute error contours for each framework.

The FNO-based approaches consistently outperform all DeepONet variants, achieving substantially lower test errors. In particular, FNO-FR demonstrates superior performance to FNO-AR for 30 and 50 training trajectories, while their accuracies remain similar at 70 and 100 trajectories. Finally, GNS achieves the best generalization performance overall, with errors below 1% (0.9% for  $u$  and

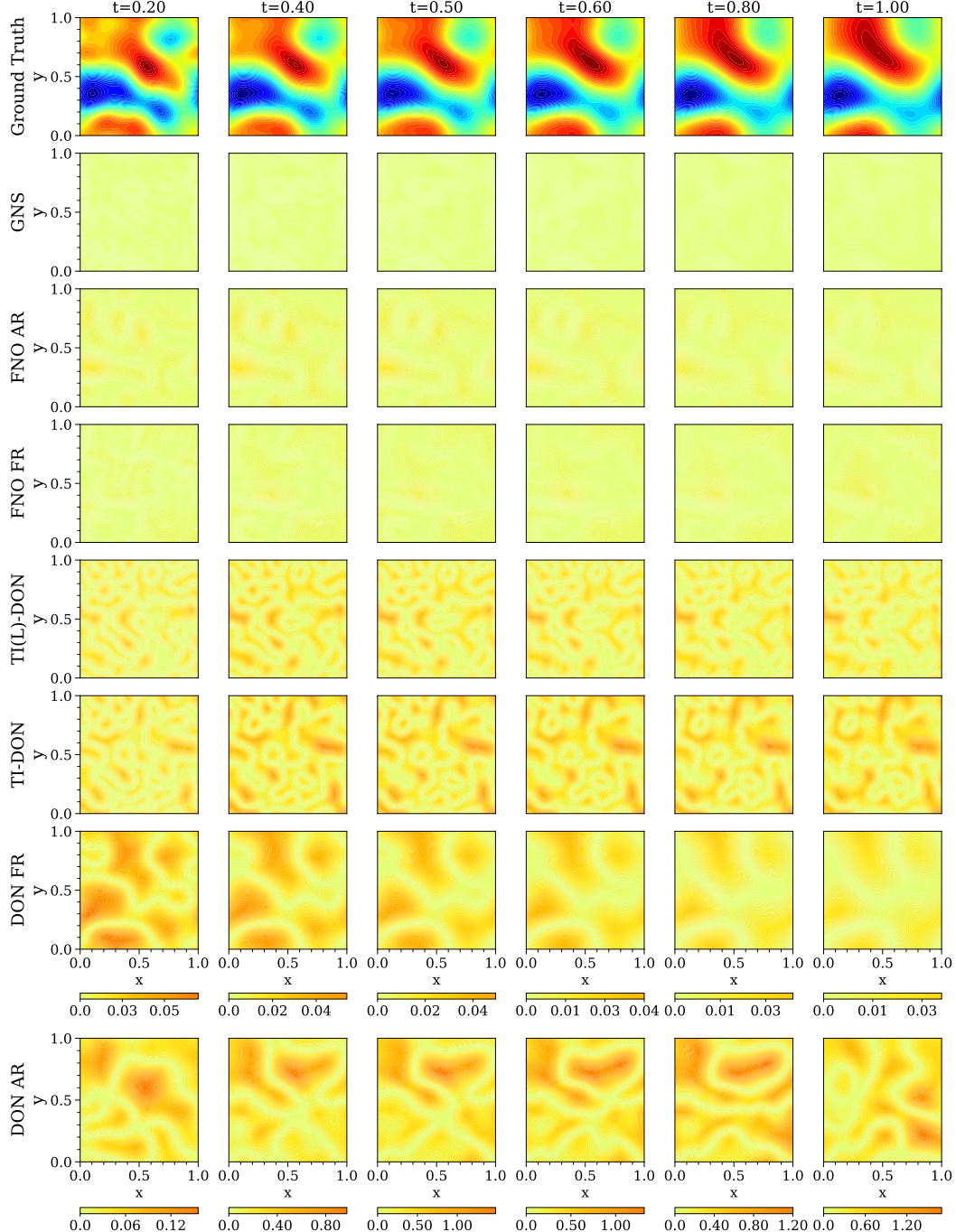


Figure 6: 2D coupled Burgers' equation with a vector field: Performance of all frameworks on 30 training trajectories, evaluated on 500 trajectories for predicting the  $v$ -velocity field of a representative sample. Top row: ground truth solution contours; subsequent rows: absolute error contours for each framework.

0.78% for  $v$ ) even when trained on only 30 trajectories. This highlights GNS's inherent ability to naturally incorporate multiple interacting fields as node features, thereby capturing spatial interactions and coupling dynamics in a physically intuitive manner. Such an inductive bias makes GNS more

Table 3: Two-Dimensional Burgers’ equation with vector output field: Inference errors for  $u$  and  $v$  fields across different methods and training trajectory counts. At inference, 500 trajectories are used, with a timestep of  $\Delta t = 0.01$  for the time-integrator-based frameworks (GNS, TI-DON, TI(L)-DON).

Method	Training Trajectories			
	30	50	70	100
Field $u$				
GNS	<b>0.0091</b>	<b>0.00539</b>	<b>0.003431</b>	<b>0.00335</b>
DON FR	0.60742	0.4325	0.32581	0.2267
DON AR	3.2	8.259	1.0125	4.3491
TI-DON	0.535	0.3957	0.34607	0.2967
TI(L)-DON	0.52753	0.40503	0.34889	0.3081
FNO AR	0.087918	0.0408109	0.0227915	0.01426
FNO FR	0.054958	0.031109	0.023148	0.0149934
Field $v$				
GNS	<b>0.0078</b>	<b>0.00549</b>	<b>0.0036</b>	<b>0.003305</b>
DON FR	0.691209	0.3939	0.32882	0.2182
DON AR	5.593	3.713	12.6281	9.1233
TI-DON	0.553	0.3947	0.33249	0.2769
TI(L)-DON	0.56157	0.395902	0.33098	0.2764
FNO AR	0.098911	0.042962	0.024126	0.015502
FNO FR	0.0499403	0.0310453	0.0227212	0.0146658

physics-aware, enabling it to learn nonlinear, complex, and coupled dynamics effectively even in the low-data regime.

### 3.3 Two-Dimensional Allen–Cahn Equation

The third example that we consider is the two-dimensional Allen–Cahn equation, which serves as a prototype model for phase separation and interface dynamics. It describes the evolution of an order parameter by balancing diffusion-driven smoothing with a nonlinear reaction term that enforces bistable equilibrium states. The governing equation is:

$$\frac{\partial u}{\partial t} = \epsilon^2 \left( \frac{\partial^2 u}{\partial x^2} + \frac{\partial^2 u}{\partial y^2} \right) - (u^3 - u), \quad \forall (x, y, t) \in [0, 1]^2 \times [0, 1], \quad (7)$$

where  $u(x, y, t)$  is a scalar order parameter field, and  $\epsilon = 0.05$  controls the interfacial width (or diffusion length). The initial condition,  $u(x, y, 0) = u_0(x, y)$ , is sampled from two-dimensional Gaussian random fields, and periodic Dirichlet and Neumann boundary conditions are imposed along both spatial directions.

Mathematically, this is a nonlinear parabolic reaction–diffusion equation. The diffusion term tends to smooth spatial variations, while the cubic reaction term,  $-(u^3 - u)$ , drives the system toward the two stable equilibrium states  $u = \pm 1$ , leading to phase separation. The resulting dynamics are characterized by the formation and motion of interfaces, which evolve approximately by mean curvature flow and give rise to metastable domain patterns. For surrogate modeling, the Allen–Cahn equation poses two key challenges: (i) the strong nonlinearity of the cubic term amplifies prediction errors in long-horizon rollouts, and (ii) the interplay between sharp interfacial layers (set by  $\epsilon$ ) and large-scale domain coarsening requires models to resolve both fine-scale structures and large-scale phase separation dynamics, demanding robustness across multiple spatial and temporal scales.

The dataset is generated by solving the two-dimensional Allen–Cahn equation on a periodic spatial domain  $[0, 1] \times [0, 1]$ , discretized using a uniform  $32 \times 32$  grid. Temporal evolution is computed up to  $T_{\text{final}} = 1.0$  using an exponential time-differencing fourth-order Runge–Kutta (ETDRK4) scheme with a coarse time step  $\Delta t = 0.01$ , refined by a factor of 200 for numerical stability. The total number of coarse snapshots is  $n_{\text{coarse}} = 101$ . Initial conditions are sampled from Gaussian-filtered

random fields and scaled to the range  $[-1, 1]$ . Specific implementation details are provided in Table 1. Training trajectory selection follows the PCA-KMeans procedure employed in all other cases.

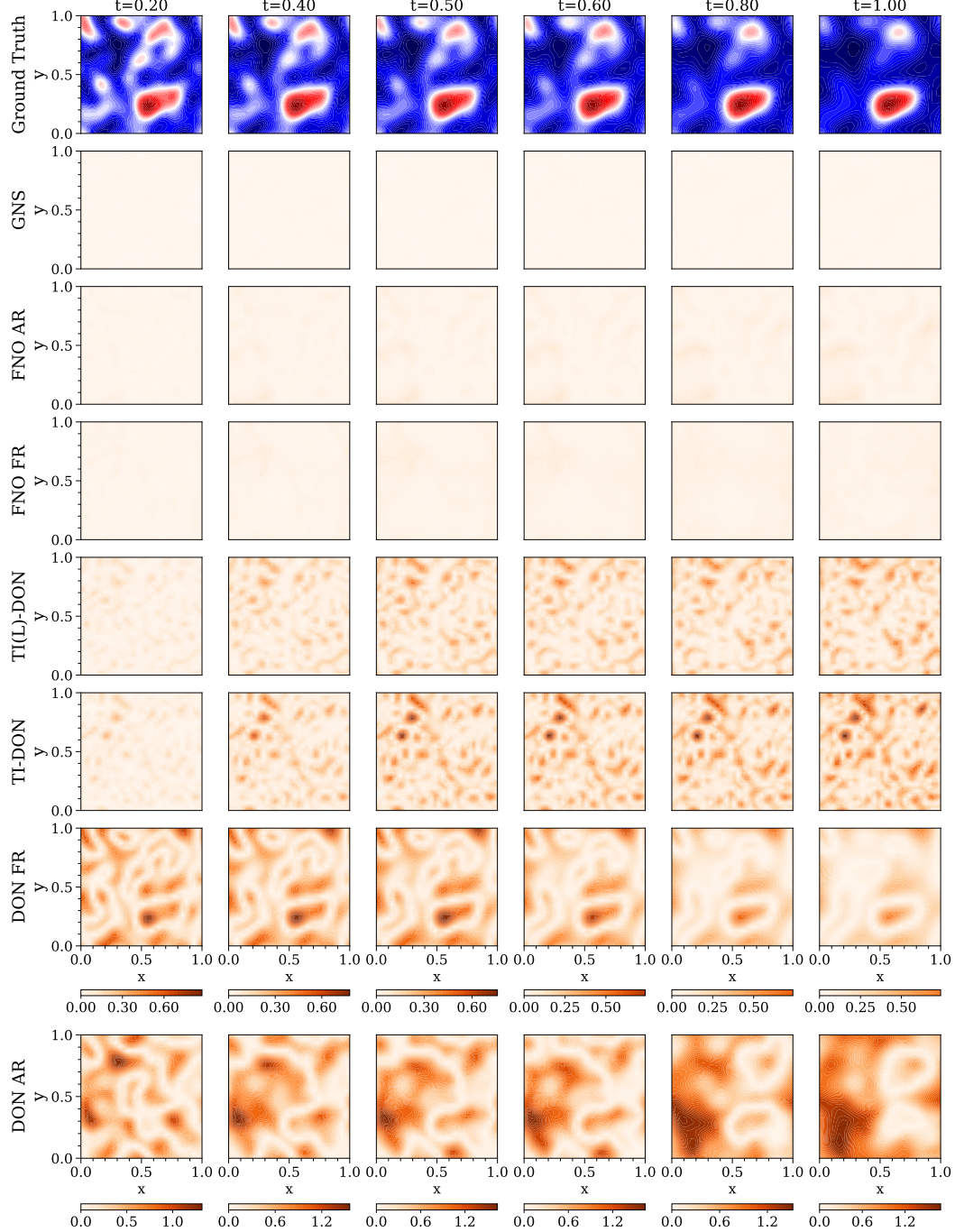


Figure 7: 2D Allen-Cahn Equation: Performance of all frameworks on 30 training trajectories, evaluated on 1000 trajectories for a representative sample. Top row: ground truth solution contours; subsequent rows: absolute error contours for each framework.

Figure 7 depicts the comparative performance of all frameworks for different time snapshots of a representative sample, using 30 training trajectories. The qualitative trends observed here are

consistent with the previous two cases. DON-AR exhibits significantly larger errors compared to all other frameworks, highlighting its sensitivity to the accumulation of model approximation errors at each timestep, which is particularly pronounced in the low-data regime. Among the remaining DeepONet-based methods, the TI variants outperform DON-FR for timesteps up to  $t = 0.6$ , after which DON-FR surpasses TI(L)-DON and TI-DON, achieving lower absolute errors. Across all timesteps, the learnable TI variant, TI(L)-DON, consistently yields lower errors due to its adaptive numerical time-stepping scheme conditioned on the solution state at each timestep. In comparison, FNO significantly outperforms all DeepONet-based frameworks, producing far lower errors and closely matching the ground truth. Between the FNO variants, FNO-FR marginally outperforms FNO-AR and approaches the high accuracy of GNS. Finally, GNS delivers solution profiles that almost perfectly match the ground truth, even with a very limited number of training trajectories (*e.g.* 30). This superior performance arises because GNS naturally captures spatial interactions and interface dynamics inherent to the Allen–Cahn equation, effectively encoding the phase separation and interfacial motion patterns as relational node features, which provides a strong inductive bias for learning complex, nonlinear dynamics in the low-data regime.

Table 4: Two-dimensional Allen-Cahn equation: Inference errors for  $u$  fields across different methods and training trajectory counts. At inference, 1000 trajectories are used, with a timestep of  $\Delta t = 0.01$  for the time-integrator-based frameworks (GNS, TI-DON, TI(L)-DON).

Method	Training Trajectories			
	30	50	70	100
GNS	<b>0.003483</b>	<b>0.003437</b>	<b>0.003399</b>	<b>0.003394</b>
DON FR	0.78454	0.673335	0.632006	0.59262
DON AR	1.34333	1.24514	1.51555	1.65602
TI-DON	0.59872	0.596406	0.55184	0.52573
TI(L)-DON	0.531176	0.53339	0.51611	0.48485
FNO AR	0.038041	0.014089	0.008046	0.004988
FNO FR	0.0213076	0.0089356	0.0070546	0.0037004

Lastly, in line with the findings from the previous two cases, we quantitatively evaluate the relative  $L_2$  test errors at inference on 1000 trajectories, training on subsets of 30, 50, 70, and 100 trajectories (see Table 4). As expected, DON-AR incurs the highest errors; however, compared to the earlier cases, the performance gap between DON-AR and the other frameworks is smaller, albeit its errors still exceed 100%. DON-FR follows with slightly better accuracy, though it remains inferior to the TI-based frameworks, *i.e.*, TI-DON and TI(L)-DON. Among these, the learnable counterpart consistently outperforms its vanilla version across all training subsets. Consistent with earlier observations, FNO significantly outperforms the DeepONet-based frameworks, achieving much lower test errors for all training subsets. Notably, both FNO-AR and FNO-FR nearly match the performance of GNS when trained on 100 trajectories. Finally, GNS once again establishes itself as the most robust and accurate framework, delivering superior performance over all others with relative errors as low as 0.4%-even with scarce training data (30 trajectories).

### 3.4 Two-Dimensional nonlinear Shallow Water Equations

The final example that we consider is the two-dimensional nonlinear shallow water equations with three coupled fields: fluid column height  $\eta(x, y, t)$  and velocity components  $u(x, y, t)$  and  $v(x, y, t)$ . These equations are derived by depth-integrating the Navier-Stokes equations under the assumption that horizontal length scales greatly exceed vertical scales. This leads to nearly hydrostatic vertical pressure gradients and depth-constant horizontal velocities, allowing the vertical velocity to be eliminated through integration. While vertical velocity is removed from the equations, it can be recovered from the continuity equation once the horizontal solution is obtained. The governing equations are:

$$\frac{\partial(\eta)}{\partial t} + \frac{\partial(\eta u)}{\partial x} + \frac{\partial(\eta v)}{\partial y} = 0, \quad (8)$$

$$\frac{\partial(\eta u)}{\partial t} + \frac{\partial}{\partial x} \left( \eta u^2 + \frac{1}{2} g \eta^2 \right) + \frac{\partial(\eta v)}{\partial y} = \nu(u_{xx} + u_{yy}), \quad (9)$$

$$\frac{\partial(\eta v)}{\partial t} + \frac{\partial(\eta u)}{\partial x} + \frac{\partial}{\partial y} \left( \eta v^2 + \frac{1}{2} g \eta^2 \right) = \nu(v_{xx} + v_{yy}). \quad (10)$$

The system is solved on the spatiotemporal domain defined as:  $(x, y) \in [0, 1] \times [0, 1]$  and  $t \in [0, 1]$ . The initial conditions are defined as follows. The total fluid column height  $\eta(x, y, t)$ , is given by a mean value of 1 plus some initial perturbation around a unit mean depth,  $\eta_0(x, y)$ . The initial velocity fields  $u(x, y, t)$  and  $v(x, y, t)$  are zero. We set the gravitational acceleration  $g = 1$  and the viscosity coefficient  $\nu = 0.002$ . This problem presents a particularly challenging benchmark that combines multiple coupled fields with complex nonlinear dynamics. The shallow water equations serve as an excellent test case due to their physical relevance in modeling tsunami propagation and other geophysical flows. Further, these equations share structural similarities with compressible fluid dynamics, differing primarily in the absence of an energy equation dependent on the equation of state.

Mathematically, the shallow water equations form a nonlinear hyperbolic system of conservation laws. The advective fluxes capture nonlinear momentum transport, while the pressure-gradient and source terms govern gravity-driven wave propagation and topographic interactions. The dynamics are characterized by the coexistence of smooth wave-like solutions and sharp gradients, including hydraulic jumps, shocks, and bore formations. This multiscale behavior leads to complex flow patterns that are highly sensitive to initial and boundary conditions. For surrogate modeling, the shallow water equations pose two key challenges: (i) the strong nonlinearity of the advective terms amplifies errors over long-horizon rollouts, particularly in the presence of shocks and discontinuities, and (ii) the simultaneous need to capture fine-scale features such as bores and fronts, alongside basin-scale wave propagation and circulation, demands models that are robust across multiple spatial and temporal scales.

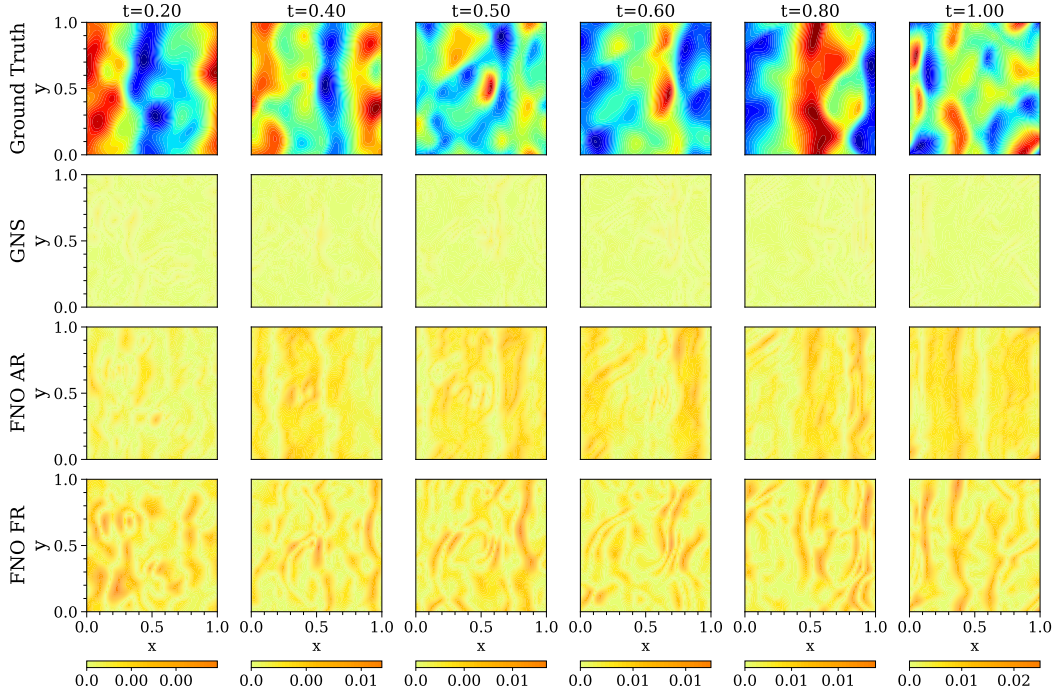


Figure 8: 2D nonlinear shallow water equations: Performance of all frameworks on 50 training trajectories, evaluated on 500 trajectories for predicting the  $u$ -velocity field of a representative sample. Top row: ground truth solution contours; subsequent rows: absolute error contours for each framework.

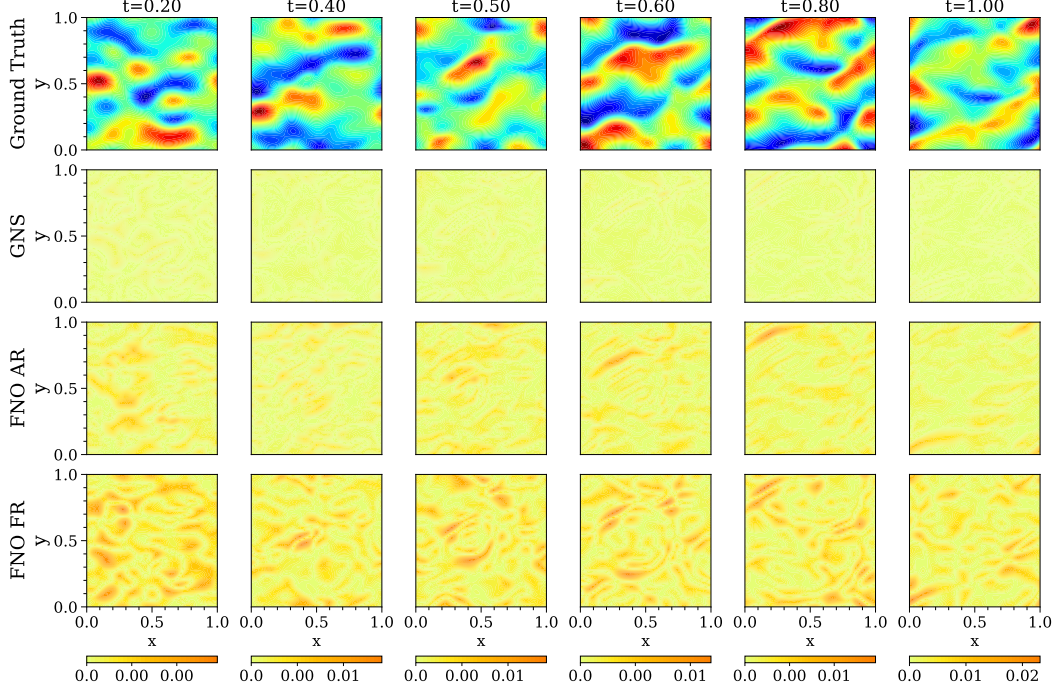


Figure 9: 2D nonlinear shallow water equations: Performance of all frameworks on 50 training trajectories, evaluated on 500 trajectories for predicting the  $v$ -velocity field of a representative sample. Top row: ground truth solution contours; subsequent rows: absolute error contours for each framework.

The ground truth dataset is generated following a strategy similar to those in cases 3.1 and 3.2. As before, the initial conditions are sampled from smooth Gaussian random fields with Matérn-type kernels and periodic boundary conditions. Once again, to pick the most informative subset of training trajectories, the PCA-KMeans procedure was employed (see Section 3.1) by retaining the first 50 dominant principal vectors following the PCA dimensionality reduction step.

We now examine the performance of different surrogates for the three coupled fields: the velocity components  $u$  and  $v$ , and the height field  $h$ . Figures 8, 9, and 10 present a qualitative comparison of prediction errors for GNS, FNO AR, and FNO FR. All methods were trained on 50 trajectories and evaluated on 500 test trajectories. Notably, the DeepONet variants exhibited poor performance on this problem, producing errors several orders of magnitude larger than the FNO variants and GNS. This degraded performance can be attributed to the initial conditions where both velocity fields  $u$  and  $v$  are exactly zero, creating a potentially challenging scenario for DeepONet’s operator learning framework. Hence, for brevity, we focus our analysis only on the comparison between GNS and the two FNO variants (FNO AR and FNO FR). Between the FNO variants, FNO FR incurs larger errors than FNO AR. This can be attributed to the inherent difficulty of the FNO FR framework in trying to learn the solution operator from near-zero initial conditions (exactly zero  $u$  and  $v$  velocity fields). GNS performs the best out of all three frameworks, with the errors in a very small range and the predictions showing a near perfect match, with a modest training set of 50 trajectories. The rationale is that in spite of the near zero initial conditions, the evolution dynamics of  $u$  and  $v$  velocity fields is effortlessly handled by GNS. Primarily in the SWE case, the initial perturbation provided to the height field is what sets up or induces the velocity fields and these nonlinear interactions are extremely well captured by GNS owing to its ability to model such interactions in a more physically-consistent manner that closely mimicks the true dynamics.

Table 5 presents a comprehensive evaluation of the relative  $L_2$  test errors for GNS and FNO-based variants trained with subsets of 30, 50, 70, and 100 trajectories. The quantitative error values exhibit strong agreement with the qualitative observations in Figs. 8, 9, and 10. Across all training subsets,

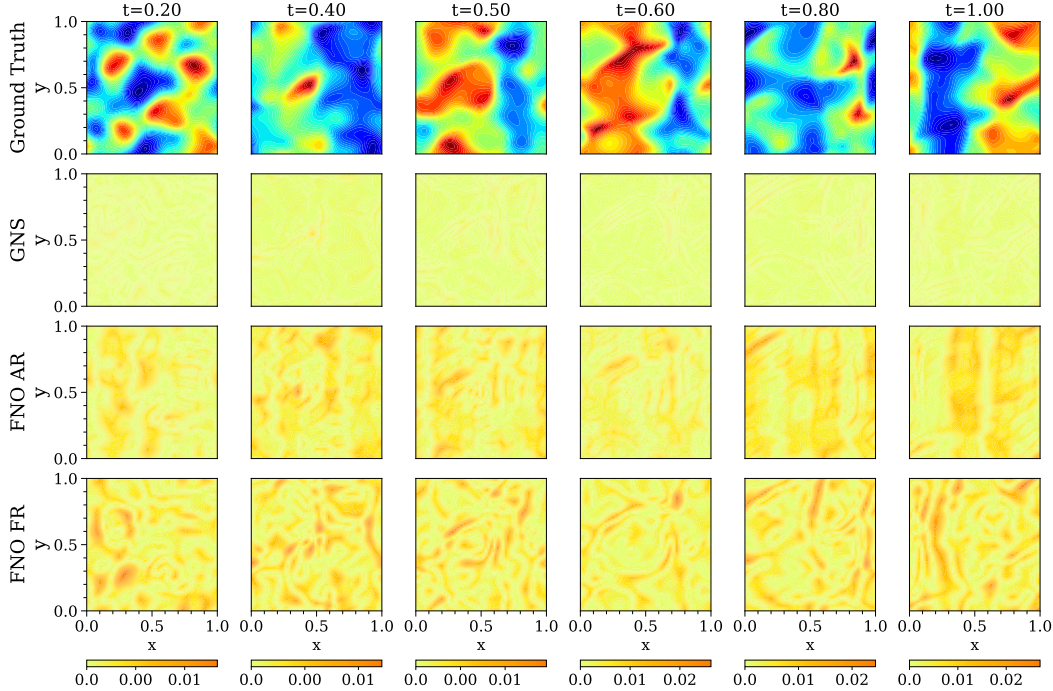


Figure 10: 2D nonlinear shallow water equations: Performance of all frameworks on 50 training trajectories, evaluated on 500 trajectories for predicting the height field,  $h$ , of a representative sample. Top row: ground truth solution contours; subsequent rows: absolute error contours for each framework.

Table 5: Two-Dimensional nonlinear shallow water equations with vector output field: Inference errors for  $u$ ,  $v$ , and  $h$  fields across different methods and training trajectory counts. At inference, 500 trajectories are used, with a timestep of  $\Delta t = 0.01$  for GNS.

Method	Training Trajectories			
	30	50	70	100
Field $u$				
GNS	<b>0.0323</b>	<b>0.01718</b>	<b>0.01175</b>	<b>0.00505</b>
FNO AR	0.0347	0.03682	0.02904	0.02366
FNO FR	0.1496	0.09056	0.06069	0.04432
Field $v$				
GNS	<b>0.0270</b>	<b>0.01916</b>	<b>0.00933</b>	<b>0.00468</b>
FNO AR	0.03562	0.03098	0.02373	0.01947
FNO FR	0.1343	0.08105	0.05415	0.03989
Field $h$				
GNS	<b>0.00074</b>	<b>0.00048</b>	<b>0.00021</b>	<b>0.00012</b>
FNO AR	0.00102	0.00097	0.00076	0.00062
FNO FR	0.00411	0.00246	0.00162	0.00117

GNS consistently delivers the best performance, achieving the lowest errors for all three coupled fields,  $u$ ,  $v$ , and  $h$ . This is closely followed by FNO AR, which has slightly higher errors than GNS but performs substantially better than FNO FR, which exhibits the highest errors across all training subsets. The primary reason for the deterioration in FNO FR performance is the underlying operator learning problem it faces: mapping near-zero initial conditions (due to initial zero velocities) to the full spatiotemporal solution field, which, as established earlier, is an especially challenging task.

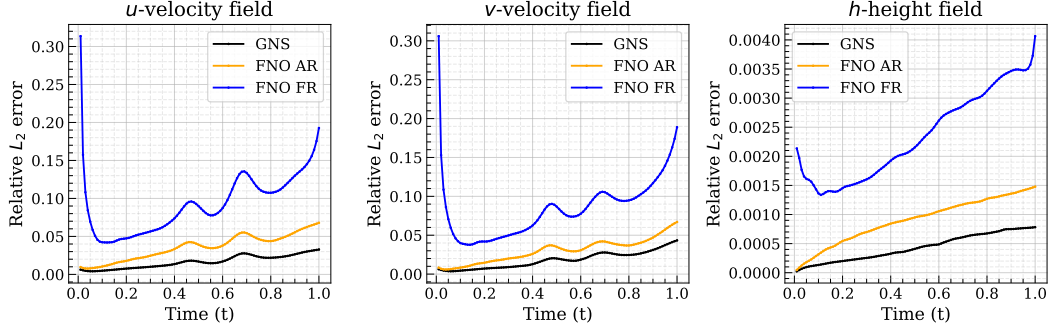


Figure 11: 2D nonlinear shallow water equations: Temporal evolution of error accumulation across GNS (black), FNO AR (orange), and FNO FR (blue).

We also assess the temporal error growth for the GNS and FNO frameworks in Fig. 11. In addition to exhibiting higher generalization accuracy in the limited-data regime, GNS (black) demonstrates stable and controlled error growth, indicating robustness and reliability in predicting accurate solutions over extended time horizons. FNO AR (orange) follows closely, while FNO FR (blue) shows comparatively higher error accumulation, consistent with the results in Table 5. Finally, the relatively large  $L_2$  errors for the  $u$  and  $v$  velocity fields in Fig. 11 for FNO FR can be attributed to the zero initial conditions and the difficulty FNO FR encounters in learning the coupling between the initial height perturbation and the subsequent evolution of the velocity fields. By contrast, GNS is able to effectively capture this coupling despite the zero initial velocity fields.

## 4 Conclusions

In this work, we performed a systematic comparison of generalization performance of various NO frameworks, including DeepONet and FNO-based variants with Graph Neural Simulators (GNS), on four representative two-dimensional PDEs: the viscous Burgers equation, the coupled Burgers system, the Allen–Cahn equation, and the nonlinear shallow water equations. Across all cases, we evaluated both qualitative solution contours and quantitative relative  $L_2$  errors under varying amounts of training data. Our results demonstrate that DeepONet-based methods are more sensitive to limited training data compared to other NOs, with DON-AR consistently exhibiting the largest errors due to the accumulation of approximation errors over time, which is further exacerbated in low-data regimes. TI-based DeepONet variants improve upon the generalization performance of DON-FR, particularly when training data is very limited. However, with sufficient training trajectories, DON-FR surpasses the TI variants due to a more accurate representation of the output solution space, enabled by the increased availability of data. FNO frameworks consistently outperform all DeepONet variants, especially for PDEs whose solutions are dominated by low-frequency modes, making them particularly amenable to spectral-space learning and enabling efficient capture of the dominant frequency modes that govern the PDE dynamics with relatively few training samples.

Notably, GNS emerges as the most robust and accurate framework across all PDEs, even in low-data regimes. Its superior performance is attributed to the explicit modeling of spatial interactions and local dynamics through graph-based node and edge feature representations, allowing it to naturally capture complex, nonlinear, and coupled phenomena such as viscous dissipation, nonlinear cross-advection, interfacial evolution, and wave-height coupling with gravity-driven free-surface flow. This inductive bias enables GNS to learn physically consistent representations, making it particularly effective for long-horizon rollouts and low-data scenarios. Overall, our study highlights the strengths and limitations of current neural operator approaches, demonstrating that while kernel integral operators such as FNO, which operate in spectral space, are highly effective for certain PDEs, graph-based architectures like GNS offer a more universal, physics-aware framework for learning spatiotemporally complex dynamics, particularly in low-data regimes.

## 5 Limitations and Future Work

While GNS emerged as the superior method in this study in terms of generalization performance for time-dependent PDEs because of its ability to learn the underlying dynamics through stronger physics-aware inductive biases, training such models comes with its own set of challenges. First, training a GNS (or more generally, a GNN) often incurs higher computational costs compared to operator learning frameworks. Furthermore, the inherent graph-based data structures required for representing inputs and outputs can impose significant memory demands, which may necessitate smaller batch sizes during training, especially under limited GPU capacity. This issue becomes more pronounced as the memory requirement scales with the number of nodal points, making highly resolved spatial domains quickly prohibitive. In this study, all GNS training was conducted on a multi-node, multi-GPU setup using PyTorch DDP, underscoring the importance of distributed training for scaling to large domains.

In this study, although the GNS framework was applied to uniform domains, it can be readily extended to non-uniform or irregular grids. A natural direction for future research lies in mesh-based simulations where the mesh itself deforms at every timestep, necessitating the use of temporal graph networks [37]. Beyond this, efforts could also focus on improving the scalability and efficiency of GNS-based approaches—for instance, through memory-efficient graph construction strategies, hierarchical or multiscale message-passing schemes, or hybrid architectures that combine the efficiency of neural operators with the physics-awareness of GNS, leading to more data-efficient models. Furthermore, embedding physics-informed constraints more seamlessly within the GNS framework presents an exciting opportunity to enhance robustness and broaden its applicability to complex, real-world scientific problems.

## Acknowledgments

The authors' research efforts were partly supported by the National Science Foundation (NSF) under Grant No. 2438193 and 2436738. The authors would like to acknowledge computing support provided by the Advanced Research Computing at Hopkins (ARCH) core facility at Johns Hopkins University and the Rockfish cluster. ARCH core facility (`rockfish.jhu.edu`) is supported by the NSF grant number OAC1920103. Any opinions, findings, conclusions, or recommendations expressed in this material are those of the author(s) and do not necessarily reflect the views of the funding organizations.

## References

- [1] Peter Benner, Serkan Gugercin, and Karen Willcox. A survey of projection-based model reduction methods for parametric dynamical systems. *SIAM review*, 57(4):483–531, 2015.
- [2] Alfio Quarteroni, Andrea Manzoni, and Federico Negri. *Reduced basis methods for partial differential equations: an introduction*, volume 92. Springer, 2015.
- [3] Stefania Fresca, Luca Dede’, and Andrea Manzoni. A comprehensive deep learning-based approach to reduced order modeling of nonlinear time-dependent parametrized PDEs. *Journal of Scientific Computing*, 87(2):61, 2021.
- [4] Stefania Fresca and Andrea Manzoni. POD-DL-ROM: Enhancing deep learning-based reduced order models for nonlinear parametrized PDEs by proper orthogonal decomposition. *Computer Methods in Applied Mechanics and Engineering*, 388:114181, 2022.
- [5] Kuan Lu, Kangyu Zhang, Haopeng Zhang, Xiaohui Gu, Yulin Jin, Shibo Zhao, Chao Fu, and Yongfeng Yang. A review of model order reduction methods for large-scale structure systems. *Shock and Vibration*, 2021(1):6631180, 2021.
- [6] Kevin Carlberg, Charbel Farhat, Julien Cortial, and David Amsallem. The GNAT method for nonlinear model reduction: effective implementation and application to computational fluid dynamics and turbulent flows. *Journal of Computational Physics*, 242:623–647, 2013.
- [7] Lu Lu, Pengzhan Jin, Guofei Pang, Zhongqiang Zhang, and George Em Karniadakis. Learning nonlinear operators via DeepONet based on the universal approximation theorem of operators. *Nature machine intelligence*, 3(3):218–229, 2021.

- [8] Somdatta Goswami, Aniruddha Bora, Yue Yu, and George Em Karniadakis. Physics-informed deep neural operator networks. In *Machine learning in modeling and simulation: methods and applications*, pages 219–254. Springer, 2023.
- [9] Bogdan Raonic, Roberto Molinaro, Tim De Ryck, Tobias Rohner, Francesca Bartolucci, Rima Alaifari, Siddhartha Mishra, and Emmanuel de Bézenac. Convolutional neural operators for robust and accurate learning of PDEs. *Advances in Neural Information Processing Systems*, 36:77187–77200, 2023.
- [10] Boris Bonev, Thorsten Kurth, Christian Hundt, Jaideep Pathak, Maximilian Baust, Karthik Kashinath, and Anima Anandkumar. Spherical fourier neural operators: Learning stable dynamics on the sphere. In *International conference on machine learning*, pages 2806–2823. PMLR, 2023.
- [11] Qianying Cao, Somdatta Goswami, and George Em Karniadakis. Laplace neural operator for solving differential equations. *Nature Machine Intelligence*, 6(6):631–640, 2024.
- [12] Zongyi Li, Nikola Kovachki, Kamyar Azizzadenesheli, Burigede Liu, Andrew Stuart, Kaushik Bhattacharya, and Anima Anandkumar. Multipole graph neural operator for parametric partial differential equations. *Advances in Neural Information Processing Systems*, 33:6755–6766, 2020.
- [13] Zongyi Li, Nikola Kovachki, Chris Choy, Boyi Li, Jean Kossaifi, Shourya Otta, Mohammad Amin Nabian, Maximilian Stadler, Christian Hundt, Kamyar Azizzadenesheli, et al. Geometry-informed neural operator for large-scale 3d pdes. *Advances in Neural Information Processing Systems*, 36:35836–35854, 2023.
- [14] Zhongkai Hao, Zhengyi Wang, Hang Su, Chengyang Ying, Yinpeng Dong, Songming Liu, Ze Cheng, Jian Song, and Jun Zhu. Gnot: A general neural operator transformer for operator learning. In *International Conference on Machine Learning*, pages 12556–12569. PMLR, 2023.
- [15] Zongyi Li, Nikola Kovachki, Kamyar Azizzadenesheli, Burigede Liu, Kaushik Bhattacharya, Andrew Stuart, and Anima Anandkumar. Fourier neural operator for parametric partial differential equations. *arXiv preprint arXiv:2010.08895*, 2020.
- [16] Sifan Wang, Hanwen Wang, and Paris Perdikaris. Learning the solution operator of parametric partial differential equations with physics-informed DeepONets. *Science advances*, 7(40):eabi8605, 2021.
- [17] Luis Mandl, Somdatta Goswami, Lena Lambers, and Tim Ricken. Separable physics-informed DeepONet: Breaking the curse of dimensionality in physics-informed machine learning. *Computer Methods in Applied Mechanics and Engineering*, 434:117586, 2025.
- [18] Luis Mandl, Dibyajyoti Nayak, Tim Ricken, and Somdatta Goswami. Physics-Informed Time-Integrated DeepONet: Temporal Tangent Space Operator Learning for High-Accuracy Inference. *arXiv preprint arXiv:2508.05190*, 2025.
- [19] Wei Wang, Maryam Hakimzadeh, Haihui Ruan, and Somdatta Goswami. Time-marching neural operator–FE coupling: AI-accelerated physics modeling. *Computer Methods in Applied Mechanics and Engineering*, 446:118319, 2025.
- [20] Levi D McClenney and Ulisses M Braga-Neto. Self-adaptive physics-informed neural networks. *Journal of Computational Physics*, 474:111722, 2023.
- [21] Somdatta Goswami, Dimitris G Giovanis, Bowei Li, Seymour MJ Spence, and Michael D Shields. Neural Operators for Stochastic Modeling of Nonlinear Structural System Response to Natural Hazards. *arXiv preprint arXiv:2502.11279*, 2025.
- [22] Kurt Hornik. Approximation capabilities of multilayer feedforward networks. *Neural networks*, 4(2):251–257, 1991.
- [23] Alex Krizhevsky, Ilya Sutskever, and Geoffrey E Hinton. Imagenet classification with deep convolutional neural networks. *Advances in neural information processing systems*, 25, 2012.
- [24] Franco Scarselli, Marco Gori, Ah Chung Tsoi, Markus Hagenbuchner, and Gabriele Monfardini. The graph neural network model. *IEEE transactions on neural networks*, 20(1):61–80, 2008.
- [25] TN Kipf. Semi-Supervised Classification with Graph Convolutional Networks. *arXiv preprint arXiv:1609.02907*, 2016.

- [26] Petar Veličković, Guillem Cucurull, Arantxa Casanova, Adriana Romero, Pietro Lio, and Yoshua Bengio. Graph attention networks. *arXiv preprint arXiv:1710.10903*, 2017.
- [27] Zonghan Wu, Shirui Pan, Fengwen Chen, Guodong Long, Chengqi Zhang, and Philip S Yu. A comprehensive survey on graph neural networks. *IEEE transactions on neural networks and learning systems*, 32(1):4–24, 2020.
- [28] Alvaro Sanchez-Gonzalez, Jonathan Godwin, Tobias Pfaff, Rex Ying, Jure Leskovec, and Peter Battaglia. Learning to Simulate Complex Physics with Graph Networks. In *International conference on machine learning*, pages 8459–8468. PMLR, 2020.
- [29] Tobias Pfaff, Meire Fortunato, Alvaro Sanchez-Gonzalez, and Peter Battaglia. Learning Mesh-Based Simulation with Graph Networks. In *International conference on learning representations*, 2020.
- [30] Justin Gilmer, Samuel S Schoenholz, Patrick F Riley, Oriol Vinyals, and George E Dahl. Neural message passing for quantum chemistry. In *International conference on machine learning*, pages 1263–1272. Pmlr, 2017.
- [31] Dibyajyoti Nayak and Somdatta Goswami. TI-DeepONet: Learnable Time Integration for Stable Long-Term Extrapolation. *arXiv preprint arXiv:2505.17341*, 2025.
- [32] Svante Wold, Kim Esbensen, and Paul Geladi. Principal component analysis. *Chemometrics and intelligent laboratory systems*, 2(1-3):37–52, 1987.
- [33] John A Hartigan and Manchek A Wong. Algorithm AS 136: A k-means clustering algorithm. *Journal of the royal statistical society. series c (applied statistics)*, 28(1):100–108, 1979.
- [34] Michael M Bronstein, Joan Bruna, Yann LeCun, Arthur Szlam, and Pierre Vandergheynst. Geometric deep learning: going beyond euclidean data. *IEEE Signal Processing Magazine*, 34(4):18–42, 2017.
- [35] Michael M Bronstein, Joan Bruna, Taco Cohen, and Petar Veličković. Geometric deep learning: Grids, groups, graphs, geodesics, and gauges. *arXiv preprint arXiv:2104.13478*, 2021.
- [36] Shawn G Rosofsky, Hani Al Majed, and E A Huerta. Applications of physics informed neural operators. *Machine Learning: Science and Technology*, 4(2):025022, may 2023.
- [37] Emanuele Rossi, Ben Chamberlain, Fabrizio Frasca, Davide Eynard, Federico Monti, and Michael Bronstein. Temporal graph networks for deep learning on dynamic graphs. *arXiv preprint arXiv:2006.10637*, 2020.

## A Computational Costs

Table A1: Computational costs of training and inference for all examples across different frameworks.

Problem	Method	Batch size	Training time (iter/sec)	$N_{test}$	Inference time (sec)
2D Burgers scalar	GNS	4	72.87	1000	181.535
	FNO FR	64	7.39		3.179
	FNO AR	64	110.13		3.058
	TI(L)-DON	32	165.53		6.559
	TI-DON	32	202.76		6.899
	DON FR	32	91.35		1.298
	DON AR	128	305.95		5.043
2D Burgers vector	GNS	4	45.63	500	199.242
	FNO FR	64	2.37		5.365
	FNO AR	64	35.12		6.206
	TI(L)-DON	32	30.15		12.457
	TI-DON	32	33.54		10.183
	DON FR	32	21.34		1.842
	DON AR	32	130.82		8.611
2D Allen Cahn	GNS	4	72.94	1000	181.277
	FNO FR	64	7.35		3.262
	FNO AR	64	92.57		3.768
	TI(L)-DON	64	127.26		6.704
	TI-DON	128	123.05		7.872
	DON FR	128	91.49		1.467
	DON AR	128	295.61		5.019
2D nonlinear SWE	GNS	2	45.79	500	334.032
	FNO FR	16	1.88		14.014
	FNO AR	16	14.79		11.034

## B Architecture Details

### B.1 Graph Neural Simulators (GNS)

Table A2: GNS architecture and training settings across different PDE examples. Here, MP refers to message passing. Each MP layer within the processor block uses LayerNorm. The multilayer perceptrons (MLPs) used within a single MP layer have two hidden layers of 64 neurons each, which is kept consistent across all examples. Finally, a “mean” aggregation operation is used in the message aggregation step for all MP layers.

Problem	Encoder	Processor	Decoder	Activation	Epochs	Batch Size
2D Burgers scalar	Node: [7,64,64] Edge: [7,64,64]	6 MP layers	[64,64,1]	GELU	600	4
2D Burgers vector	Node: [8,64,64] Edge: [8,64,64]	6 MP layers	[64,64,2]	GELU	400	4
2D Allen Cahn	Node: [7,64,64] Edge: [7,64,64]	6 MP layers	[64,64,1]	GELU	500	4
2D nonlinear SWE	Node: [9,64,64] Edge: [9,64,64]	6 MP layers	[64, 64, 3]	GELU	600	2

## B.2 Fourier Neural Operator (FNO)-based variants

Table A3: FNO architecture and training settings across different PDE examples. Except for the 2D nonlinear SWE case, where 6 Fourier blocks are used, all other cases use 4 Fourier blocks.

Problem	Method	Modes	Hidden Dim	Activation	Epochs	Batch Size
2D Burgers scalar	FNO AR	16	32	GELU	5000	64
	FNO FR	16	32	GELU	5000	64
2D Burgers vector	FNO AR	16	32	GELU	2000	64
	FNO FR	16	32	GELU	5000	64
2D Allen Cahn	FNO AR	16	32	GELU	4000	64
	FNO FR	16	32	GELU	5000	64
2D nonlinear SWE	FNO AR	16	64	GELU	2000	16
	FNO FR	16	64	GELU	6000	16

## B.3 Deep Operator Network (DeepONet)-based variants

Table A4: 2D Burgers' equation scalar: DeepONet architecture and training settings across different methods.

Method	Branch Net	Trunk Net	Activation	Epochs	Batch Size
TI(L)-DON	Conv2D(64, (3,3), 1), MaxPool((2,2), (2,2)), Conv2D(64, (2,2), 1), AvgPool((2,2), (2,2)), MLP([256, 128, 128, 100])	[128]*7 + [100]	Conv2D: GELU, MLP: Tanh	$2.25 \times 10^5$	32
TI-DON	Conv2D(64, (3,3), 1), MaxPool((2,2), (2,2)), Conv2D(64, (2,2), 1), AvgPool((2,2), (2,2)), MLP([256, 128, 128, 100])	[128]*7 + [100]	Conv2D: GELU, MLP: Tanh	$2 \times 10^5$	32
DON FR	Conv2D(64, (3,3), 1), MaxPool((2,2), (2,2)), Conv2D(64, (2,2), 1), AvgPool((2,2), (2,2)), MLP([256, 128, 128, 100])	[128]*7 + [100]	Conv2D: GELU, MLP: SiLU	$2 \times 10^5$	32
DON AR	Conv2D(64, (3,3), 1), MaxPool((2,2), (2,2)), Conv2D(64, (2,2), 1), AvgPool((2,2), (2,2)), MLP([256, 128, 128, 100])	[128]*7 + [100]	Conv2D: GELU, MLP: Tanh	$2 \times 10^5$	128

Table A5: 2D Burgers' equation vector: DeepONet architecture and training settings across different methods.

Method	Branch Net	Trunk Net	Activation	Epochs	Batch Size
TI(L)-DON	Conv2D(64, (3,3), 1), MaxPool((2,2), (2,2)), Conv2D(64, (2,2), 1), AvgPool((2,2), (2,2)), MLP([256, 128, 128, 100])	[128]*7 + [100]	Conv2D: GELU, MLP: Tanh	$1.75 \times 10^5$	32
TI-DON	Conv2D(64, (3,3), 1), MaxPool((2,2), (2,2)), Conv2D(64, (2,2), 1), AvgPool((2,2), (2,2)), MLP([256, 128, 128, 100])	[128]*7 + [100]	Conv2D: GELU, MLP: Tanh	$1.5 \times 10^5$	32
DON FR	Conv2D(64, (3,3), 1), MaxPool((2,2), (2,2)), Conv2D(64, (2,2), 1), AvgPool((2,2), (2,2)), MLP([256, 128, 128, 100])	[128]*7 + [100]	Conv2D: GELU, MLP: SiLU	$1.5 \times 10^5$	32
DON AR	Conv2D(64, (3,3), 1), MaxPool((2,2), (2,2)), Conv2D(64, (2,2), 1), AvgPool((2,2), (2,2)), MLP([256, 128, 128, 100])	[128]*7 + [100]	Conv2D: GELU, MLP: Tanh	$1.5 \times 10^5$	32

Table A6: 2D Allen–Cahn equation: DeepONet architecture and training settings across different methods.

Method	Branch Net	Trunk Net	Activation	Epochs	Batch Size
TI(L)-DON	Conv2D(64, (3,3), 1), MaxPool((2,2), (2,2)), Conv2D(64, (2,2), 1), AvgPool((2,2), (2,2)), MLP([256, 128, 128, 100])	[128]*7 + [100]	Conv2D: GELU, MLP: Tanh	$2.25 \times 10^5$	64
TI-DON	Conv2D(64, (3,3), 1), MaxPool((2,2), (2,2)), Conv2D(64, (2,2), 1), AvgPool((2,2), (2,2)), MLP([256, 128, 128, 100])	[128]*7 + [100]	Conv2D: GELU, MLP: Tanh	$2 \times 10^5$	128
DON FR	Conv2D(64, (3,3), 1), MaxPool((2,2), (2,2)), Conv2D(64, (2,2), 1), AvgPool((2,2), (2,2)), MLP([256, 128, 128, 100])	[128]*7 + [100]	Conv2D: GELU, MLP: SiLU	$2 \times 10^5$	128
DON AR	Conv2D(64, (3,3), 1), MaxPool((2,2), (2,2)), Conv2D(64, (2,2), 1), AvgPool((2,2), (2,2)), MLP([256, 128, 128, 100])	[128]*7 + [100]	Conv2D: GELU, MLP: Tanh	$2 \times 10^5$	128

## C Additional Results

### C.1 2D Burgers' Equation with Scalar Field

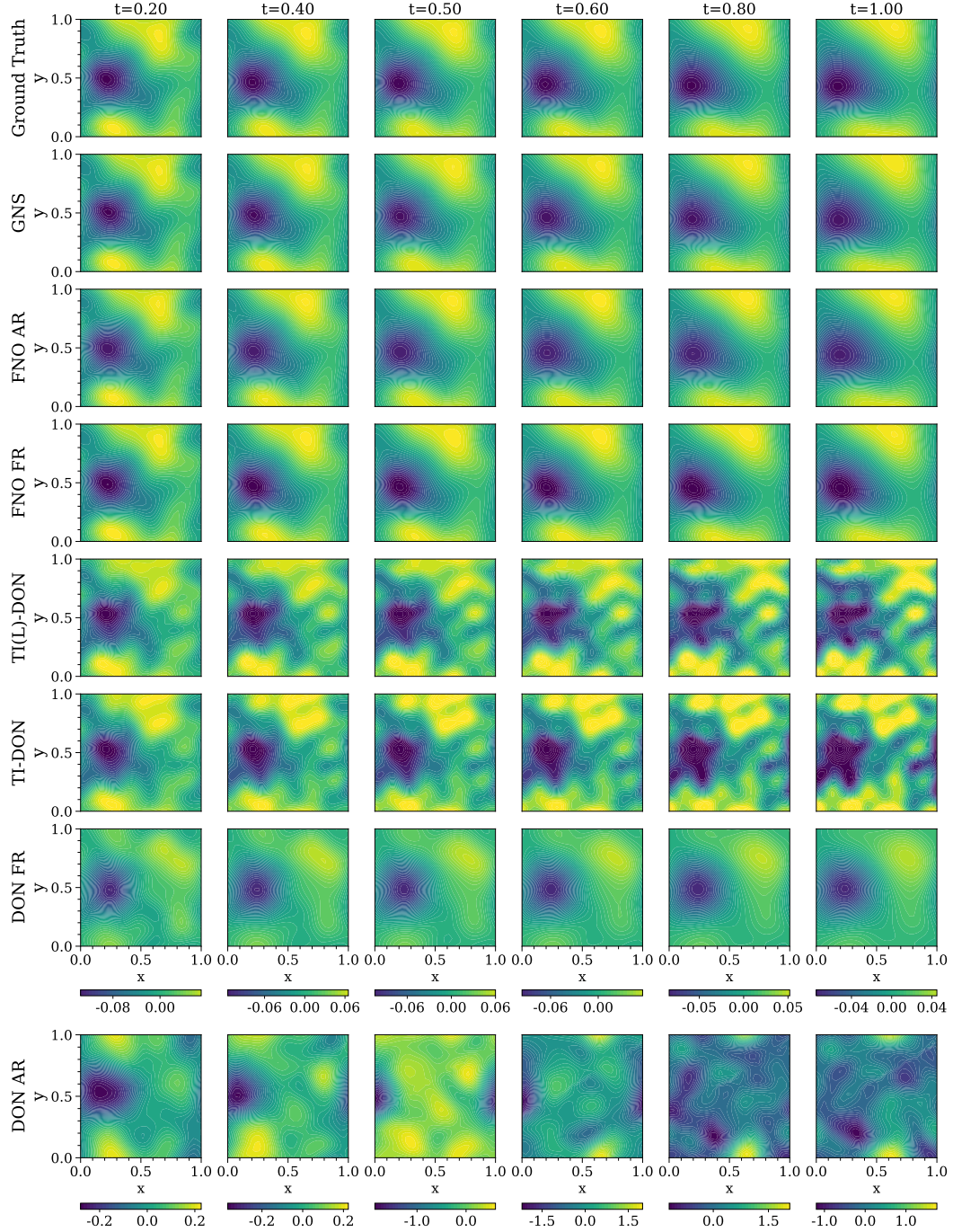


Figure A1: 2D Burgers' equation with a scalar field: Predicted solution contours of all frameworks on 30 training trajectories, evaluated on 1000 trajectories for a representative sample.

## C.2 2D Burgers' Coupled Equation with Vector Field

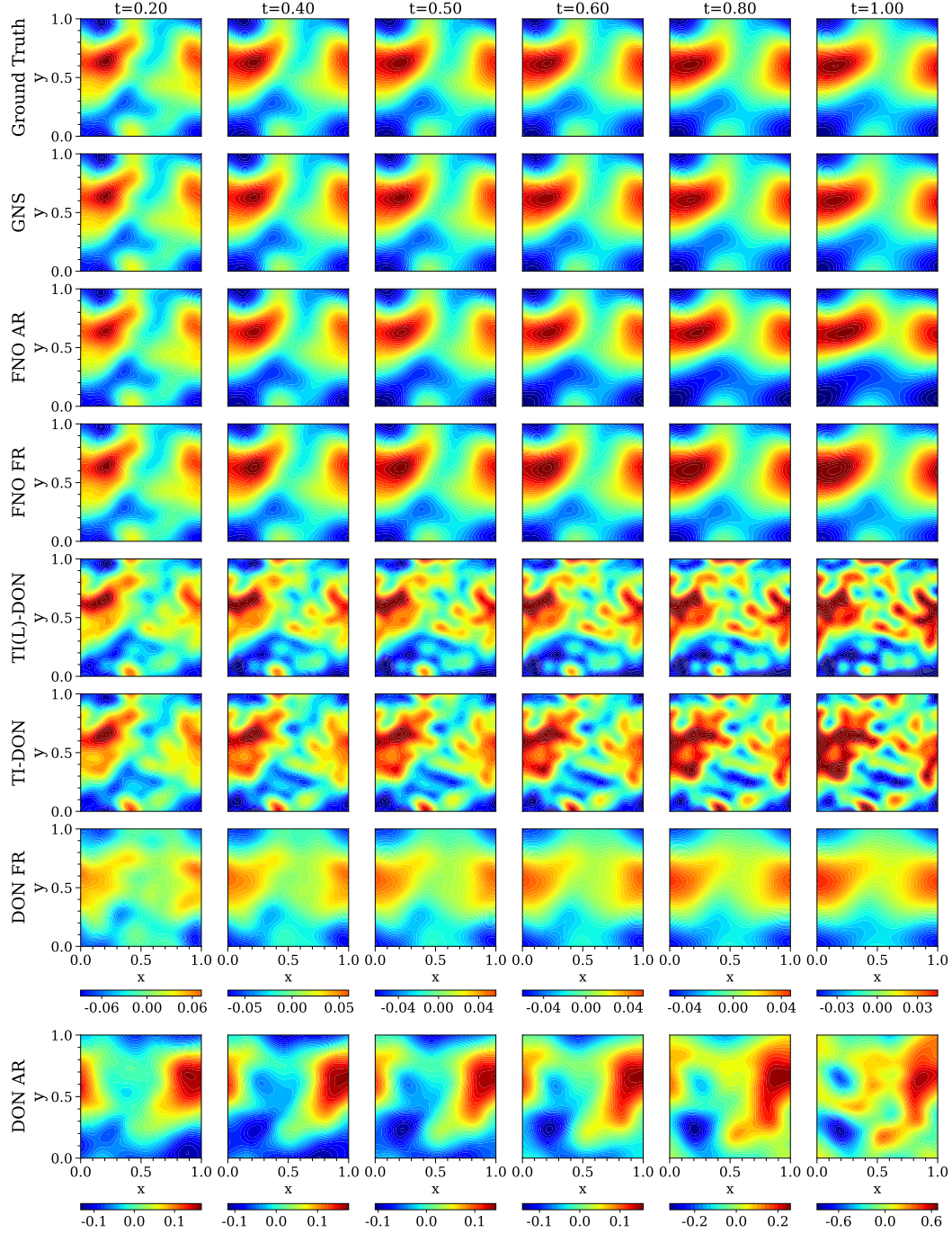


Figure A2: 2D coupled Burgers' equation with a vector field: Predicted solution contours of all frameworks on 30 training trajectories, evaluated on 1000 trajectories for predicting the  $u$ -velocity field of a representative sample.

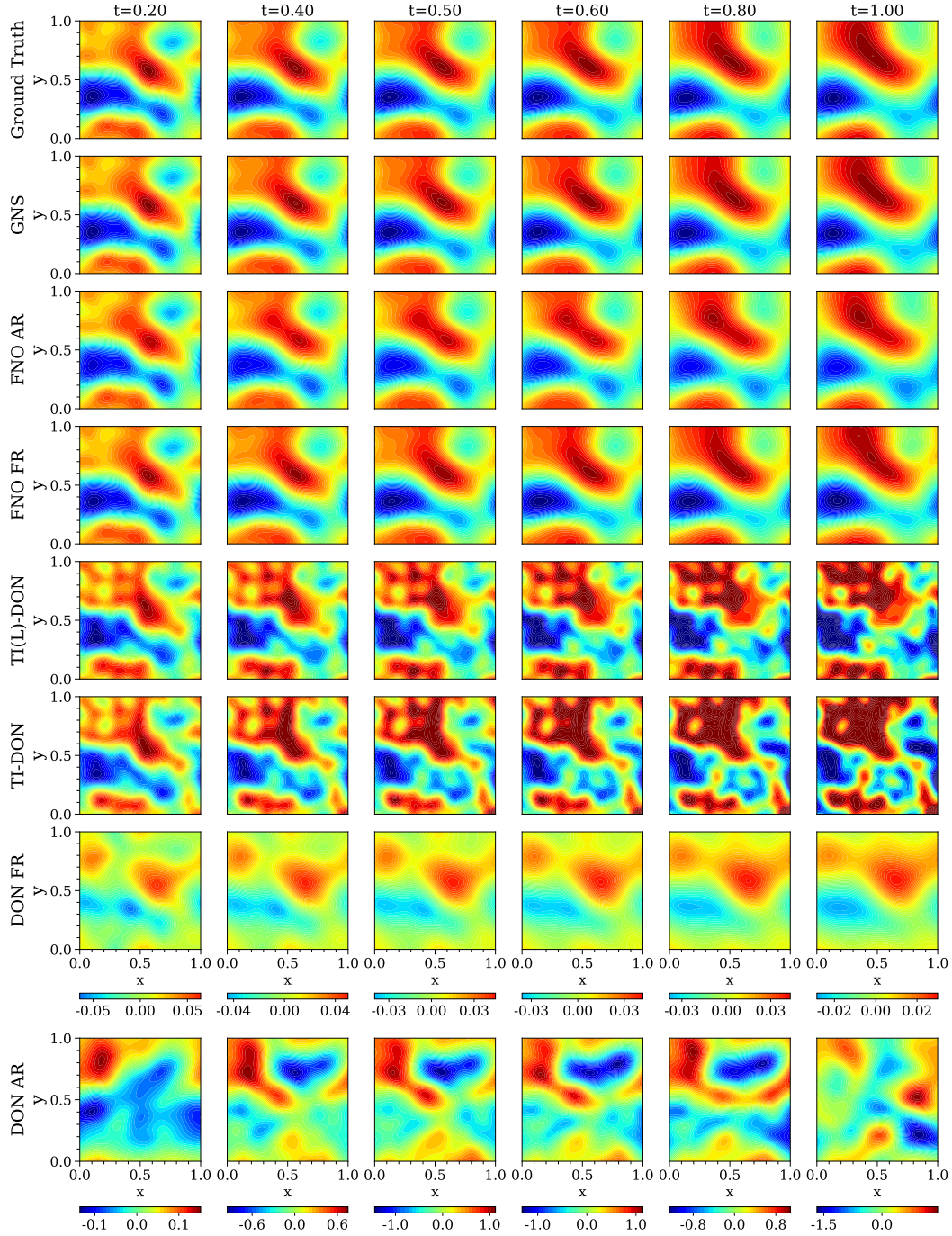


Figure A3: 2D coupled Burgers' equation with a vector field: Predicted solution contours of all frameworks on 30 training trajectories, evaluated on 1000 trajectories for predicting the  $v$ -velocity field of a representative sample.

### C.3 2D Allen-Cahn Equation

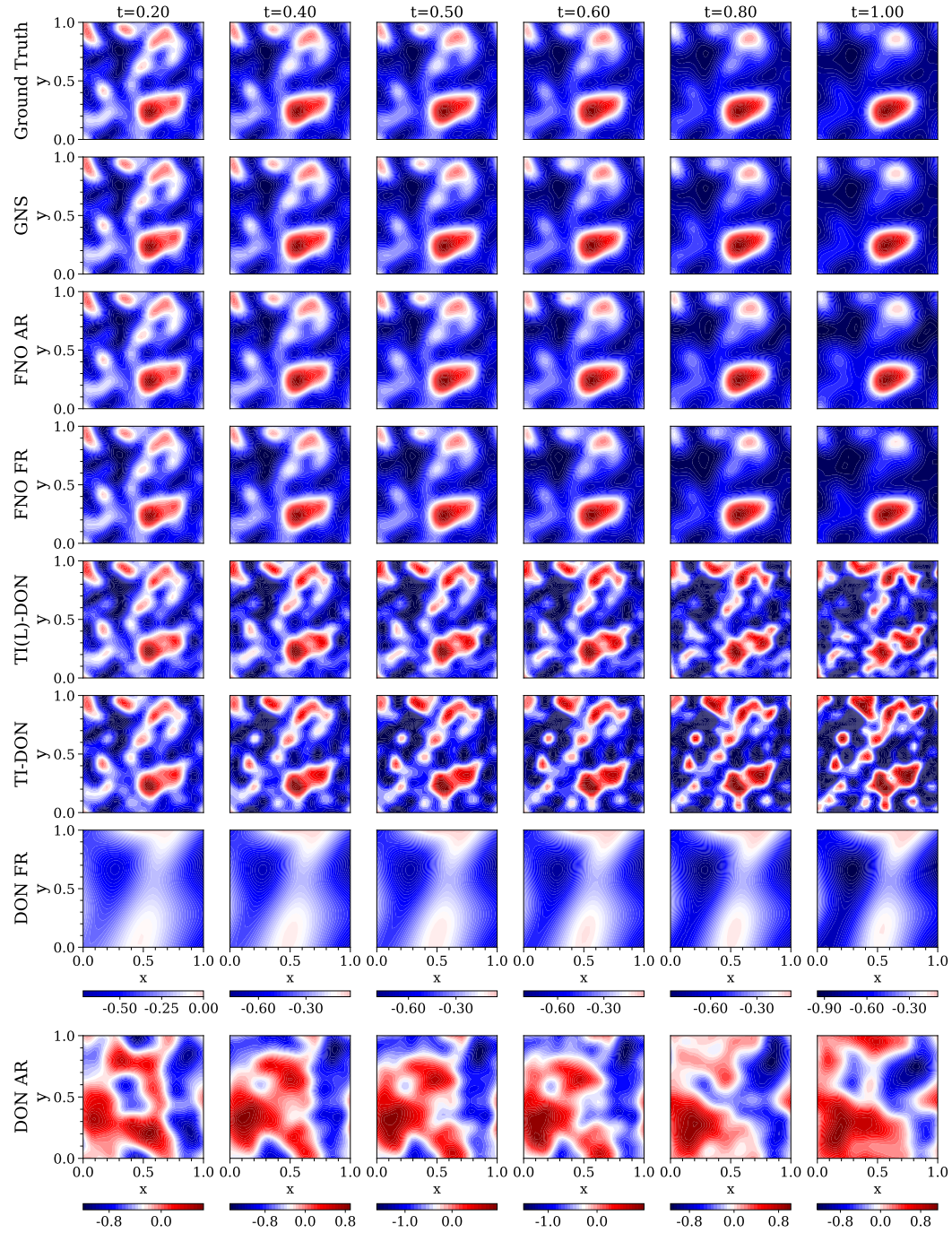


Figure A4: 2D Allen-Cahn Equation: Predicted solution contours of all frameworks on 30 training trajectories, evaluated on 1000 trajectories for a representative sample.

#### C.4 2D nonlinear Shallow Water Equations

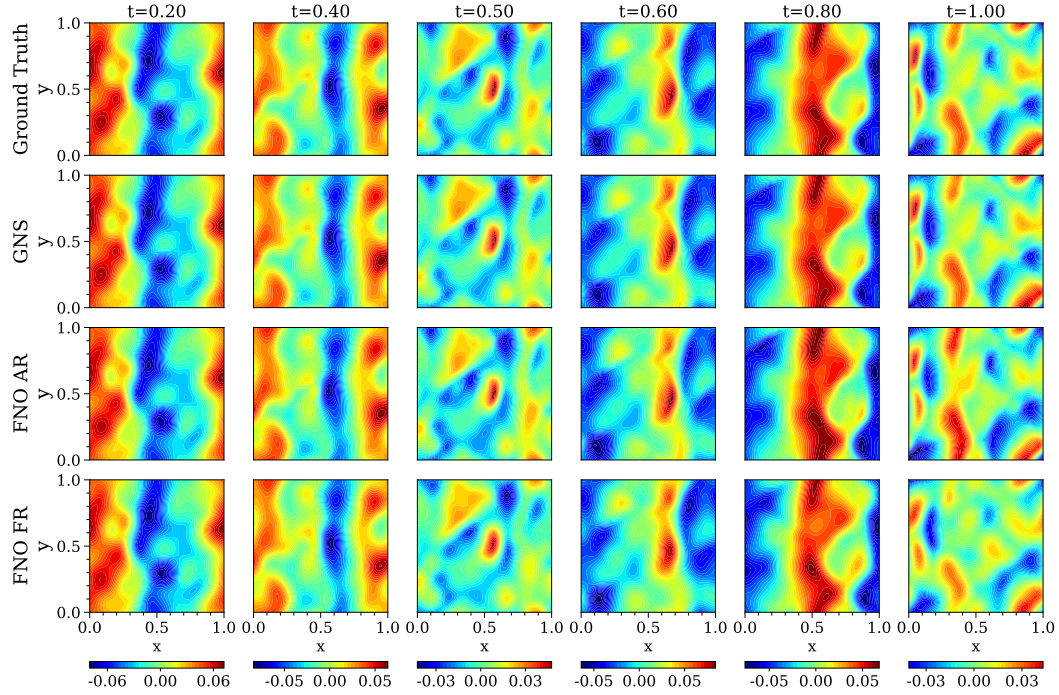


Figure A5: 2D nonlinear shallow water equations: Predicted solution contours of all frameworks on 50 training trajectories, evaluated on 500 trajectories for predicting the  $u$ -velocity field of a representative sample.

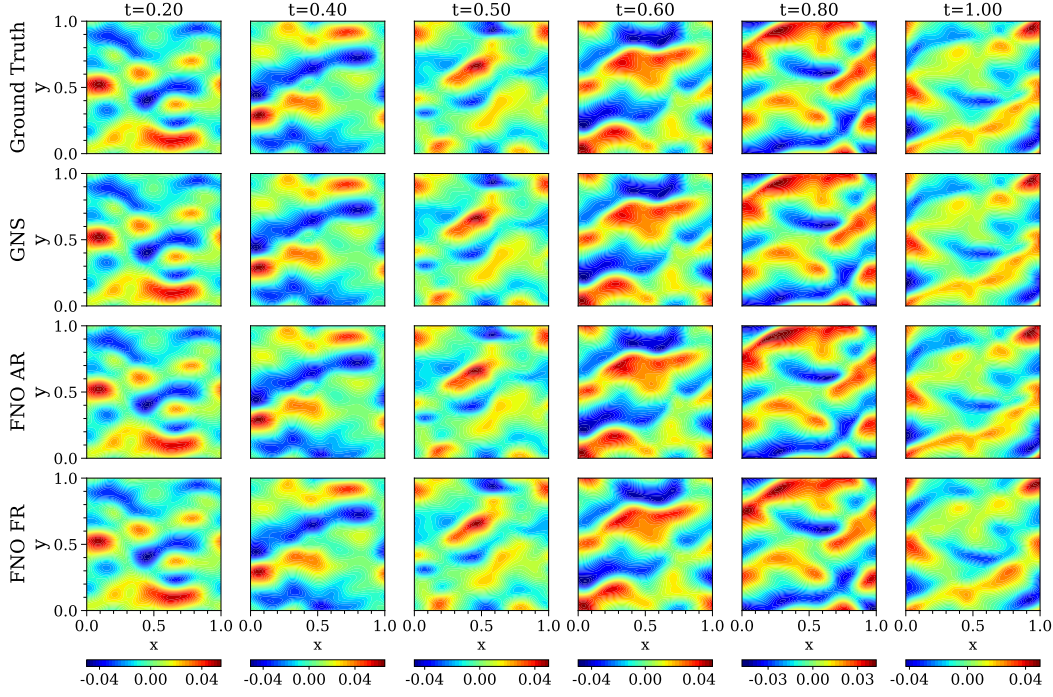


Figure A6: 2D nonlinear shallow water equations: Predicted solution contours of all frameworks on 50 training trajectories, evaluated on 500 trajectories for predicting the  $v$ -velocity field of a representative sample.

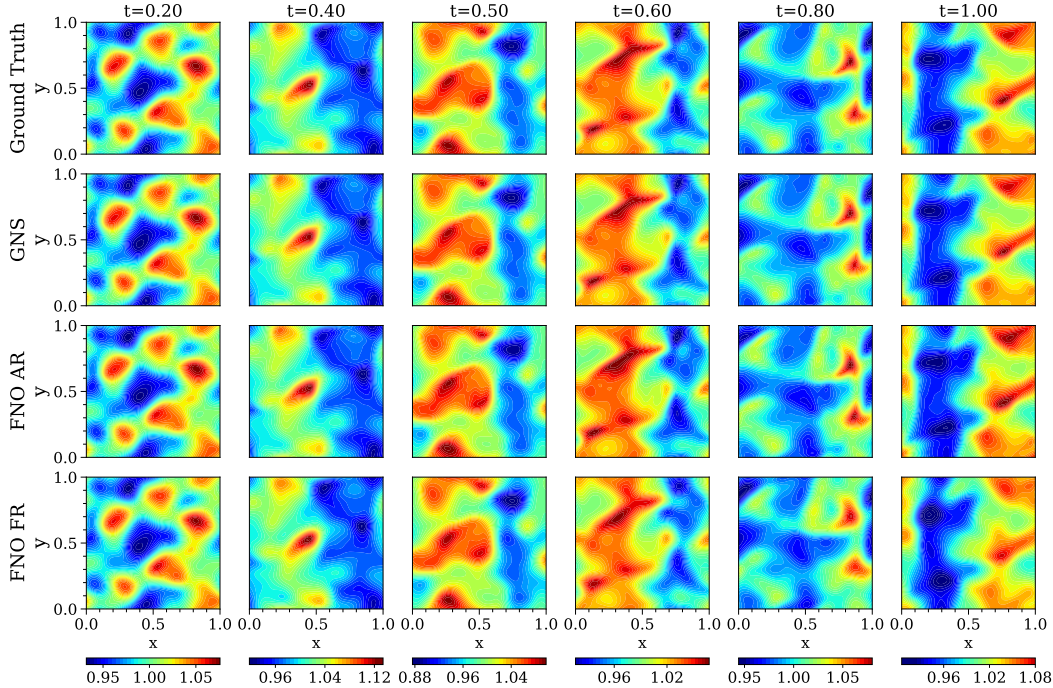


Figure A7: 2D nonlinear shallow water equations: Predicted solution contours of all frameworks on 50 training trajectories, evaluated on 500 trajectories for predicting the height field,  $h$ , of a representative sample.